Galunisertib promotes bevacizumab-induced vascular normalization in nasopharyngeal carcinoma: Multi-parameter MRI evaluation

Jing Yu,[1,6] Xia Du,[1,6] Shuai Zhang,[1] Jinhua Long,[2] Peng Wu,[3] Zongxue Li,[1] Xinyue Lyu,[1] Qin Hong,[4] Pengyu Chen,[1] and Bo Gao[1,5]

[1]Department of Radiology, The Affiliated Hospital of Guizhou Medical University, Guiyang 550004, Guizhou Province, China; [2]Department of Head & Neck, The Affiliated Tumor Hospital of Guizhou Medical University, Guiyang 550004, Guizhou Province, China; [3]Philips Healthcare, Shanghai 200072, China; [4]Department of Pathology, Guizhou Provincial People's Hospital, Guiyang 550001, Guizhou Province, China; [5]Key Laboratory of Brain Imaging, Guizhou Medical University, Guiyang 550004, Guizhou Province, China

Tumor vascular normalization (TVN) is associated with anti-tumor therapeutic efficacy in nasopharyngeal carcinoma (NPC). However, the short time window of TVN is the biggest hindrance to its wide clinical application. We investigated whether targeting transforming growth factor beta can enhance the TVN effect of bevacizumab (BEV)-induced patient-derived xenograft (PDX) models of NPC. We constructed mouse subcutaneous PDX models of NPC and classified the mice into four drug-treatment groups, namely placebo control, galunisertib, BEV, and galunisertib + BEV. We performed MRI multi-parameter examinations at different time points and evaluated the vascular density, vascular structure, and tumor hypoxia microenvironment by histopathology. The efficacy of chemotherapy and drug delivery was evaluated by administering cisplatin. We found that combined therapy with galunisertib and BEV significantly delayed tumor growth, enhanced the TVN effect, and improved chemotherapeutic efficacy compared with monotherapy. Mechanistically, galunisertib reversed the epithelial-mesenchymal transition process and inhibited the expression of hypoxia-inducible factor 1α and vascular endothelial growth factor by downregulating LAMC2. Correlation analysis of MRI data and pathological indicators showed that there was a good correlation between them.

INTRODUCTION

Nasopharyngeal carcinoma (NPC) represents the malignant head and neck tumor that originates from nasopharyngeal epithelial tissues, its occurrence mainly distributed across Southeast Asia and southern China. It is a serious threat to humans. Over 70% of patients with NPC are initially diagnosed with locally advanced stage III or IV cancer.[1] The standard treatment for patients with locally advanced NPC involves the simultaneous administration of cisplatin (DDP) chemotherapy and radiotherapy,[2] but the clinical efficacy of chemoradiotherapy alone is not satisfactory.[3] Many researchers have found that anti-angiogenesis therapy is a promising antitumor treatment.

Vascular endothelial growth factor (VEGF) is an important angiogenic factor, and bevacizumab (BEV), a human recombinant VEGF monoclonal antibody, is widely used in clinical practice. Anti-angiogenesis therapy facilitates tumor vascular normalization (TVN), thus alleviating tumor hypoxia and reshaping the tumor microenvironment (TME). These changes improve the sensitivity of tumor radiotherapy and chemotherapy, resulting in a good prognosis for patients with advanced NPC.[4–6] However, some studies have shown that the anti-VEGF-induced TVN effect is transient and has a small "time window." After this time window is closed, tumor hypoxia and acidosis are aggravated again, and the remodeling effect of the TME and the synergistic effect of antitumor therapy also end.[7] The short TVN time window for anti-angiogenesis therapy is the biggest hindrance to its wide clinical application. Therefore, various combined treatment strategies need to be investigated to achieve an effective, long-term, and stable TVN time window.[8]

Re-establishing angiogenesis regulatory balance might extend the time window of the TVN effect.[9,10] Transforming growth factor beta (TGFB) strongly influences tumor proliferation, angiogenesis, migration, invasion, and resistance to therapy.[11,12] It is an important target for tumor therapy.[13–15] Whether TGFB acts as a pro-angiogenic factor or an anti-angiogenic factor depends on the cellular environment of tumor cells and endothelial cells.[16–19] Although many preclinical studies have reported that inhibiting the TGFB pathway inhibits tumor growth and tumor cell migration and invasion,[20–24] the effect of the TGFB pathway on angiogenesis and vascular normalization in NPC is still unclear. Considering the importance of the TGFB pathway in angiogenesis, it might be a key target for overcoming anti-angiogenesis treatment resistance in NPC and, thus,

enhancing the TVN effect. Administering radiotherapy and chemotherapy during the TVN time window can effectively improve the antitumor effect.[25] Thus, it is necessary to closely monitor the rapid changes in TVN for the clinical application of combination therapy. Because the histopathological examination is invasive and non-repeatable, it is difficult to monitor the dynamic TVN process in clinical application. Magnetic resonance imaging (MRI) can be used to repeatedly and dynamically measure the morphology and function of the target within a short time.[26] Therefore, it is a suitable technique for evaluating vascular changes.[27]

In this study, we explored whether the TGFB receptor type I kinase inhibitor galunisertib (LY2157299) could improve the BEV-induced TVN effect and extend the time window in NPC patient-derived xenograft (PDX) models, thus suppressing cancer development and enhancing the efficacy of chemotherapy by alleviating tumor hypoxia and remodeling the TME. We also conducted a preliminary investigation of its mechanism and assessed the application value of combining dynamic contrast-enhanced (DCE)-MRI (K^{trans}), intravoxel incoherent motion (IVIM)-MRI (f and D^*), and amide proton transfer (APT)-MRI multi-modal MRI technology to dynamically monitor the efficacy of TVN and the response of the tumor to therapy. Our findings might contribute to the clinical transformation of anti-angiogenesis therapy.

RESULTS

High levels of TGFB1 predicted shorter survival of HNSCC cases

To determine the effect of TGFB1 on the prognosis of head and neck squamous cell carcinoma (HNSCC), the differences in the TGFB1 gene between normal and pan-cancer samples in The Cancer Genome Atlas (TCGA) were analyzed using TIMER. The TGFB1 expression in HNSCC was significantly different from that of matched normal samples ($p < 0.001$) (Figure S1A). We performed Kaplan-Meier analysis on 566 TCGA-HNSCC samples using the survival package. The samples were categorized as high-expression or low-expression groups in accordance with the median level of TGFB1. The prognosis was significantly worse in the group showing high TGFB1 expression compared to the group showing low TGFB1 expression ($p = 0.026$) (Figure S1B). We also analyzed the relationship between TGFB1 and clinical factors and found significant differences in the TGFB1 gene level in tumor stages T1, T2 and T3, and T4 ($p = 0.02$) (Figure S1C), which indicated that the TGFB1 gene level was related to the T stage of HNSCC, and there was a difference between the groups. To further evaluate the expression of TGFB1 in NPC tissues, we performed immunohistochemical staining of clinical NPC sections. Samples were gathered from 41 patients who underwent nasopharyngeal tissue biopsy without treatment; there were 23 NPC samples and 18 non-carcinoma nasopharyngeal epithelial samples. Patient characteristics are shown in Table S1. The results demonstrated that the level of TGFB1 in the NPC tissues was significantly higher than that in non-carcinoma nasopharyngeal epithelial samples ($p = 0.0322$) (Figure S1D). Our findings suggested that TGFB1 might be an anti-NPC therapeutic target.

Galunisertib synergistically enhanced the antitumor effect of BEV

To assess the antitumor effects of galunisertib on NPC, we used an NPC PDX mouse model (Figure 1). The results showed that galunisertib, BEV, and galunisertib + BEV inhibited tumor growth (Figures 2A and 2B). After 25 days of treatment, the mean tumor size in the galunisertib, BEV, and galunisertib + BEV groups was significantly smaller than that in the control group, and the mean tumor size in the galunisertib + BEV combined treatment group was smaller than that in the galunisertib or BEV monotherapy group. These results suggested that the antitumor effect of combined therapy was better than that of monotherapy.

The proliferation and apoptosis of tumor cells were further examined by immunohistochemistry. The results of the immunohistochemistry assay also showed that the antitumor effect of galunisertib + BEV combined therapy was significantly better than that of monotherapy. After the tumor-bearing mice were treated for 25 days, the number of Ki67-positive cells and the staining intensity in NPC tissues of the combined treatment group were significantly lower than that in the control group, galunisertib group, and BEV monotherapy group (Figures 2C and 2D). The findings of the TUNEL staining assay demonstrated that tumor cell apoptosis in the combination treatment group was significantly higher than that in the control group and other monotherapy groups (Figures 2E and 2F). The mouse liver, kidneys, and spleen were dissected to conduct histological analyses. The H&E-stained sections showed complete tissue structure and no cytotoxic effects in the four groups (Figure 2G). Combined targeted therapy of TGFB and VEGF had greater antiproliferative and pro-apoptotic effects and lower toxicity in NPC cells than single targeted therapy.

Galunisertib synergistically promoted the TVN of BEV

Some studies have shown that TVN is associated with improved survival rates and therapeutic outcomes in NPC patients.[28,29] To determine whether galunisertib inhibits tumor growth by synergistically promoting TVN of BEV, we evaluated the tumor microvascular density (MVD) and vascular normalization indicators (pericyte coverage index [PCI] and collagen IV) over time. Immunohistochemical staining of the endothelial cell marker CD31 showed that MVD in the three different treatment groups decreased relative to the control group. The inhibitory effect of galunisertib + BEV on tumor angiogenesis was significantly better than that of galunisertib or BEV monotherapy 14 and 25 days after treatment. Galunisertib also effectively inhibited the angiogenesis of NPC tumors after day 3, although the inhibitory effect was less than that of BEV monotherapy and galunisertib + BEV combination therapy (Figure 3A).

We further analyzed the TVN in different treatment groups. A higher PCI value represents an increase in vascular maturity and vascular normalization, which indicates vascular structure normalization. α-Smooth muscle actin (α-SMA) can specifically label perivascular cells that cover mature blood vessels.[30] Collagen IV is an important part of the vascular basement membrane and also indicates vascular
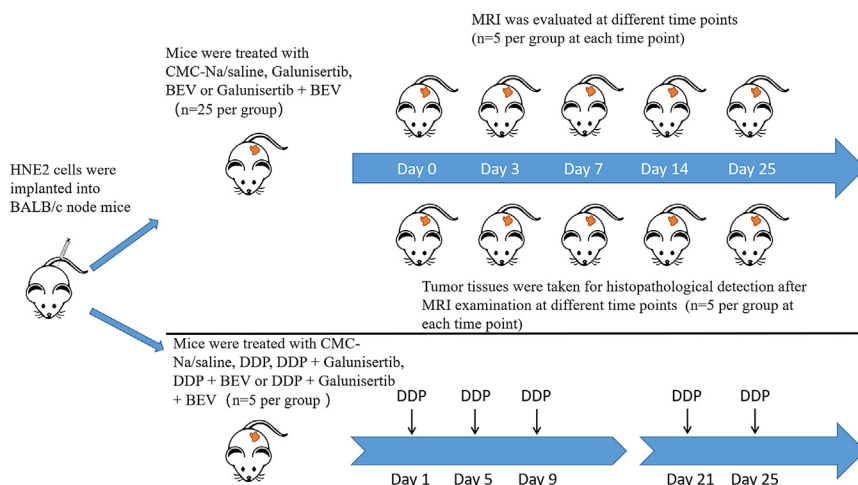
structure normalization. The results showed that the PCI and collagen IV levels in tumor tissues were lower in all groups before treatment. The PCI and collagen IV levels in NPC tumors treated with galunisertib, BEV, and galunisertib + BEV increased significantly on day 3 after intervention and reached a peak value on day 7. The increase in PCI and collagen IV levels in the combined treatment group was significantly greater than that in the single treatment group, and the decrease was slow. The PCI and collagen IV levels in the combined treatment group were higher than those of the control group and its baseline level on day 25. However, the increase in PCI and collagen IV in the monotherapy groups started decreasing rapidly from the 7th day after treatment and continued decreasing until the 14th day after treatment. The levels were close to the baseline level on the 25th day, and the difference was not significant relative to their levels in the control group (Figures 3B and 3C). Therefore, the TVN effect induced by galunisertib and BEV monotherapy started on day 3 and ended on day 14 after treatment. The TVN effect induced by galunisertib + BEV lasted from day 3 to at least day 25 after treatment, and the degree of TVN effect in the galunisertib + BEV group was significantly higher than that in the monotherapy groups.

Galunisertib inhibited HIF-1α expression in the tumor microenvironment

Since hypoxia-inducible factor 1α (HIF-1α) is strongly regulated by the concentration of oxygen in cells, which partially reflects the degree of hypoxic microenvironment of tumors, we examined the expression of HIF-1α in the tumors of different treatment groups by immunofluorescence. The findings demonstrated that after 25 days of treatment, the HIF-1α level in the galunisertib + BEV group was considerably lower than that in the control group, whereas it was higher in the BEV monotherapy group (Figure 4A). These findings suggested that galunisertib + BEV combined therapy significantly improved the anoxic microenvironment of the tumor, whereas BEV monotherapy did not improve but worsened the anoxic state of the tumor after 25 days of treatment. The expression of HIF-1α in the galunisertib monotherapy group decreased after 25 days of treatment, but the difference was not significant

compared to its expression in the combination group ($p = 0.2429$) (Figure 4A). However, these results were contrary to the results of TVN indicators. Based on these findings, we speculated that galunisertib might directly regulate the HIF-1α level in tumor hypoxia. Considering that HIF-1α strongly influences tumor microenvironment remodeling and angiogenesis and that VEGF is the most important angiogenic factor, we designed four *in vitro* cell experiments with a control group, TGFB1 (20 ng/mL) group, galunisertib (8 μM) group, and TGFB1 (20 ng/mL) + galunisertib (8 μM) group. The results of the western blotting assay showed that galunisertib inhibited HIF-1α and the expression of VEGF induced by TGFB1 in NPC cells (Figure 4B).

Galunisertib combined with BEV enhanced the efficacy of chemotherapy

Considering that the effect of TVN can improve the hypoxia and acidosis of tumors and promote the formation of a microenvironment that is conducive to the delivery of chemotherapeutic drugs, we investigated whether the galunisertib + BEV combination therapy-induced TVN can improve the delivery efficiency and effect of the chemotherapeutic drugs. As chemotherapeutic drugs are toxic, we treated mice with a low dose of DDP (1 mg/kg) combined with different treatment regimens (DDP, DDP + galunisertib, DDP + BEV, and DDP + galunisertib + BEV). Low-dose DDP did not have a significant antitumor effect on NPC xenografted tumors, and DDP + galunisertib and DDP + BEV improved the efficacy of low-dose DDP by improving vascular functions and anoxia in the tumor microenvironment. The combination therapy of DDP + galunisertib + BEV significantly delayed tumor growth and increased the anticancer activity of non-toxic low-dose DDP in NPC (Figure 5A). The accumulation of DDP in the tumor area was detected by immunohistochemical staining 24 h after the last DDP administration. Compared to the DDP, DDP + galunisertib, and DDP + BEV groups, the DDP + galunisertib + BEV combined treatment group had significantly greater accumulation of DDP in the perivascular region of the tumor (Figures 5B and 5C). These results indicated that galunisertib + BEV combined therapy promoted the delivery of small-molecule chemotherapeutic drugs through a more durable and efficient TVN effect and improved the antitumor effect of DDP.
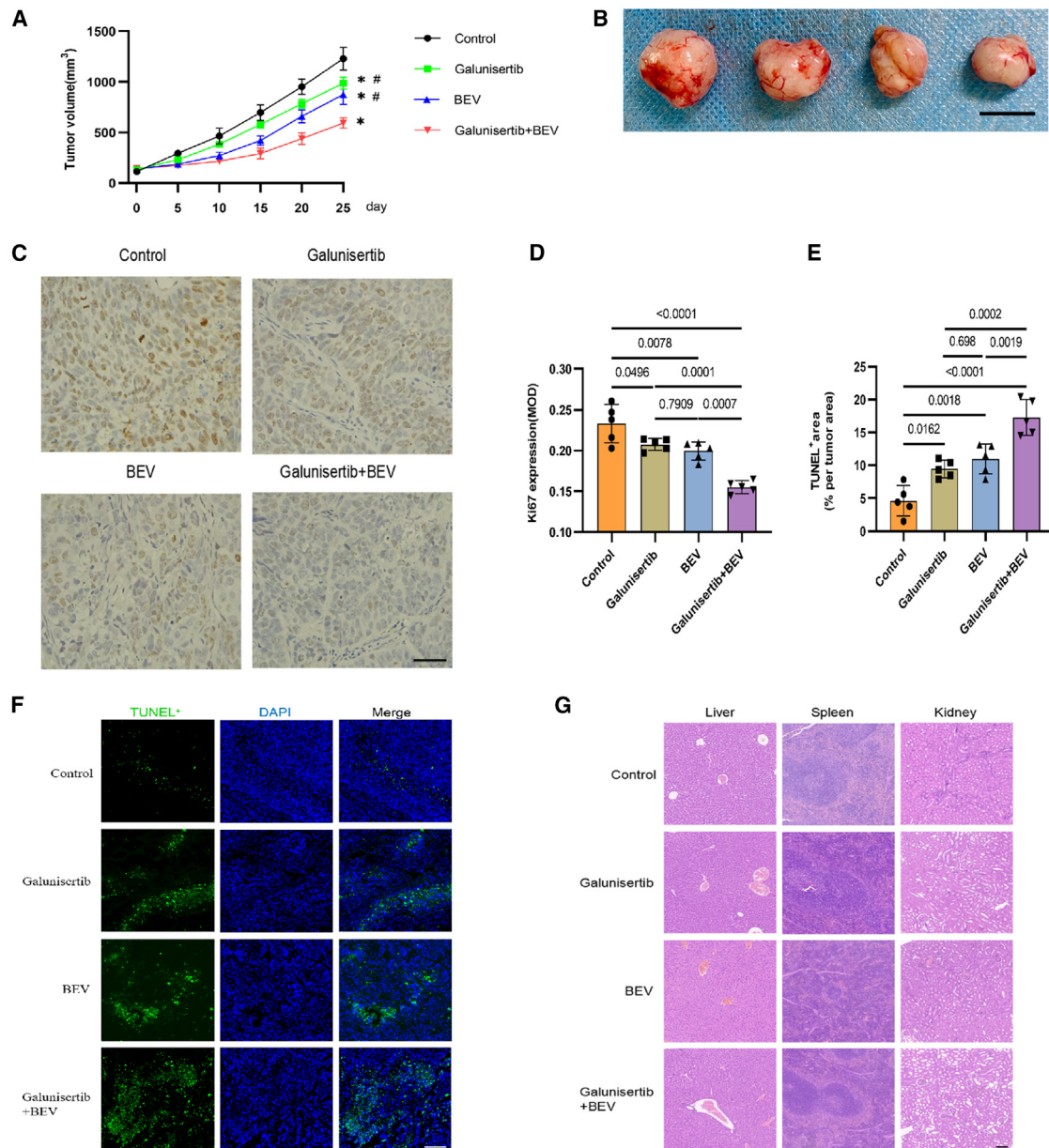
Figure 2. The effect of different treatments on tumor development, tumor cell proliferation, and apoptosis

(A) Tumor-size evaluation of NPC xenograft tumor models in different treatment groups. $n = 5$ per group at each time point; *$p < 0.05$ versus control; #$p < 0.05$ versus the galunisertib + BEV group. The p values are shown in Table S3. (B) Representative images of tumor size after 25 days of intervention in different groups. Scale bar, 10 mm. (C) Typical images of Ki67 immunohistochemically stained tumor tissues in different groups. Scale bar, 50 μm. (D) Analysis of the expression of Ki67. $n = 5$ per group. (E) Results of the TUNEL staining assay. $n = 5$ per group. (F) Representative images of TUNEL-stained NPC tumor cells in different groups. Scale bar, 50 μm. (G) Representative images of H&E-stained mouse liver, kidneys, and spleen in different treatment groups. Scale bar, 100 μm.

Galunisertib showed antitumor effects *in vitro*

To examine the impacts of galunisertib on the growth of NPC cells, different doses of galunisertib were added to treat HNE2 and HK1 cells, after which cell proliferation was assessed in all groups by the Cell Counting Kit-8 (CCK8) assay. The results of the CCK8 assay demonstrated that galunisertib inhibited the growth of NPC cells in a time-dependent and dose-dependent manner, but their IC$_{50}$ values at 24, 48, and 72 h were greater than 160 μM (Figure 6A), which suggested that in the concentration range used in our *in vivo* experiment, galunisertib had no significant cytotoxic effect on NPC cells.
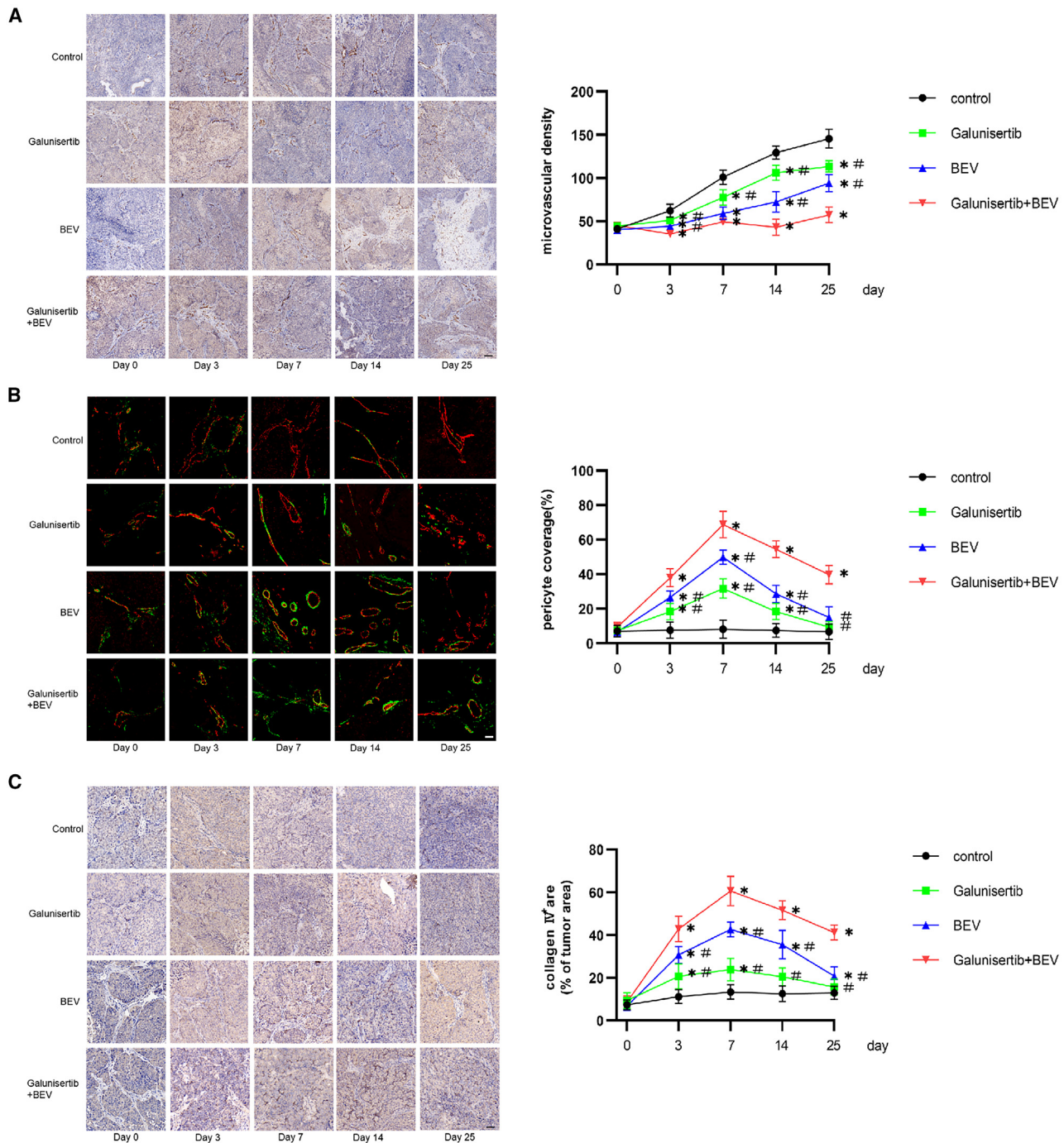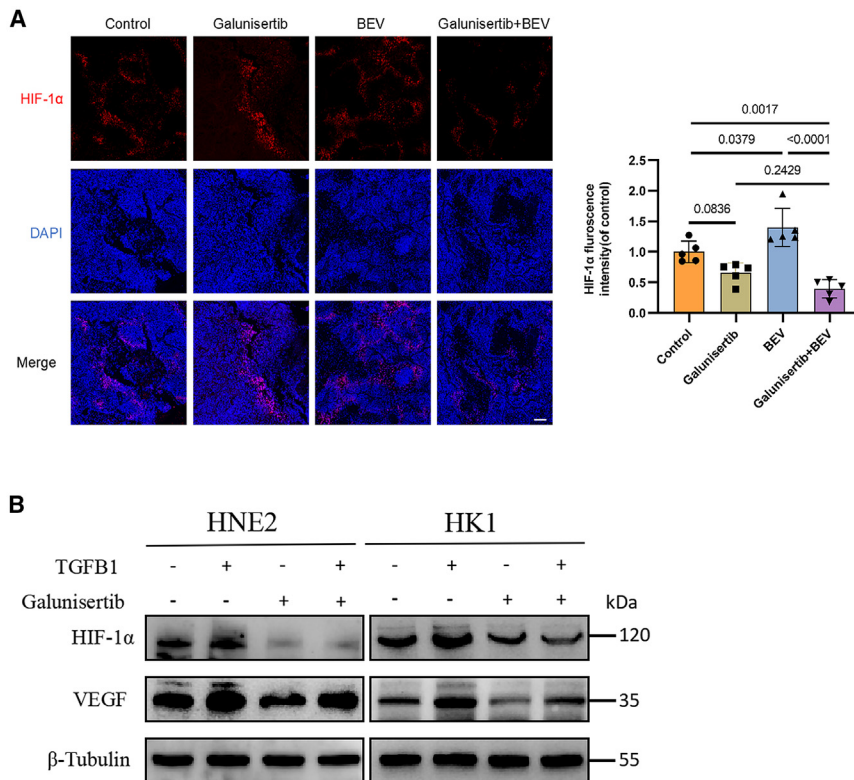
Figure 3. Histological analysis of TVN in different time periods with different treatment methods

(A) Representative images of CD31 staining and the results of microvascular density count. Scale bar, 100 μm. (B) Typical images of CD31/α-SMA immunofluorescence double staining and analysis of pericyte coverage. Scale bar, 25 μm. (C) Typical images of collagen IV staining and analysis of results. Scale bar, 50 μm. For (A)–(C), $n = 5$ per group at each time point; *$p < 0.05$ versus control; #$p < 0.05$ versus the galunisertib + BEV group. The p values are shown in Table S4.

Since the malignant phenotype of NPC is associated with cell invasion and migration, we further investigated the effect of galunisertib on the invasion and migration of NPC cells. The HNE2 and HK1 cells were treated with different concentrations of galunisertib (0, 1, 2, 4, and 8 μM), respectively. A wound-healing assay was used to detect the changes in the migration of NPC cells. The

Figure 4. HIF-1α levels in cancer tissues and cells with different treatments

(A) Representative images of HIF-1α immunofluorescence-stained cancer samples in different treatment groups and result analysis. $n = 5$ per group; Scale bar, 100 μm. (B) Western blotting assays were performed to determine the role of galunisertib in inhibiting HIF-1α and VEGF levels. The quantitative analysis of western blotting is shown in Figure S3A. β-Tubulin served as the loading control.

Galunisertib reversed the EMT process and inhibited the expression of HIF-1α and VEGF by downregulating LAMC2

We further investigated the mechanism by which galunisertib reversed the EMT process in NPC cells. The TGFB pathway mainly mediates extracellular matrix (ECM) remodeling in the TME.[31] Laminin, the main component of ECM, is located outside the cell and strongly regulates cell attachment. LAMC2, the laminin 332 (Ln-332) subunit, is an important component of the epithelial basement membrane, which modulates cell movement and adhesion. TCGA database analysis showed that the TGFB1 levels were positively correlated with LAMC2 in human HNSCC tissues ($r = 0.475$, $p < 0.001$) (Figure S2A). Our results showed that LAMC2 was related to the prognosis of HNSCC patients. The results of the Kaplan-Meier analysis showed that the upregulation of LAMC2 was significantly associated with shorter overall survival in HNSCC cases ($p = 0.023$) (Figure S2B). The findings of the pan-cancer analysis indicated that the LAMC2 gene level was notably different between the HNSCC samples and the matched normal samples ($p < 0.001$) (Figure S2C).

To determine the relationship between LAMC2 and TGFB1 in NPC, we analyzed the expression of LAMC2 and TGFB1 in NPC tumor tissues and non-cancerous nasopharyngeal epithelial samples through immunohistochemical staining in clinical specimens. Our results demonstrated that the LAMC2 levels in NPC tissues were higher than those in non-cancerous nasopharyngeal epithelial samples (Figure S2D), and the expression of TGFB1 and LAMC2 was positively correlated in NPC tissues (Figure S2E). The results of our *in vivo* experiments showed that LAMC2 expression in tumor tissue decreased in both the monotherapy group and the combined therapy group after 25 days of treatment, and the level of LAMC2 decreased most significantly in the combined therapy group (Figure S2F). We confirmed these findings via *in vitro* cell experiments. Five experimental groups were designed, which included the control, TGFB1 (20 ng/mL), galunisertib (8 μM), TGFB1 + galunisertib, and TGFB1 + TGFB1 neutralizing antibody (1 μg/mL) groups. The results of the western blotting assay showed

results demonstrated that compared to the blank control group, the galunisertib treatment group showed slower cell migration 24 h after treatment, and wound spacing was significantly widened, i.e., the cell migration ability decreased; the difference between the groups was significantly greater after 48 h. Therefore, galunisertib significantly suppressed the migration of NPC cells at low concentrations in a time-dependent manner (Figures 6B and 6C). To further examine the effect of galunisertib on the invasion of NPC cells, we conducted a Transwell assay for detecting changes in the migration of HNE2 and HK1 cells after treatment with TGFB1 (20 ng/mL) and galunisertib (8 μM) in different groups after 48 h. According to the results, after TGFB1 stimulation, the number of HNE2 and HK1 cells that entered the inferior compartment increased considerably relative to the blank control group but decreased significantly after galunisertib intervention (Figures 6D and 6E). These results suggested that galunisertib can reverse the TGFB1-induced invasion of NPC cells. The epithelial-mesenchymal transition (EMT) processes are usually related to invasion and migration, and they can also promote angiogenesis by increasing the expression of angiogenic factors. Western blotting analysis was conducted to identify the three most important EMT proteins, i.e., E-cadherin, vimentin, and N-cadherin. The results demonstrated that after TGFB1 stimulation, E-cadherin levels in the HNE2 and HK1 cells decreased, while N-cadherin and vimentin levels elevated in a dose-dependent manner (Figure 6F). The TGFB inhibitor galunisertib reversed this process (Figure 6G).
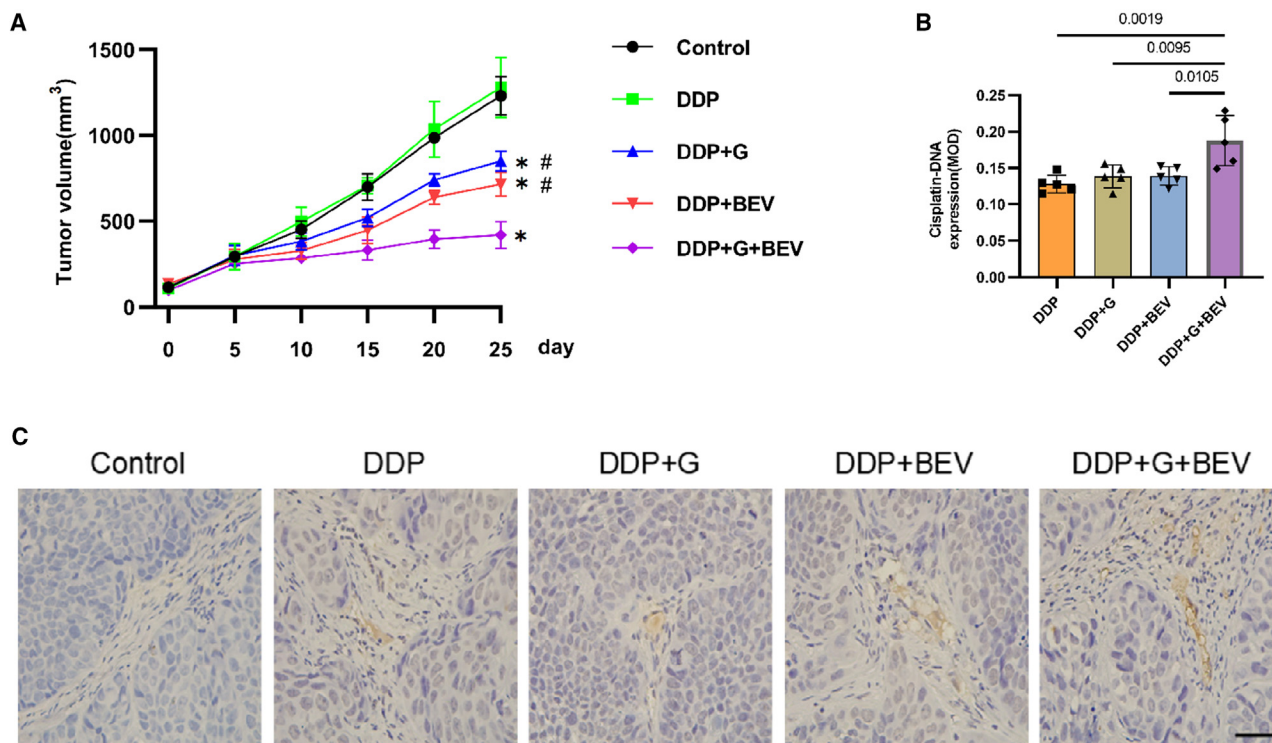
Figure 5. Effects of different treatment regimens on the sensitivity and therapeutic efficacy of the chemotherapeutic drug DDP for NPC

(A) Tumor-size evaluation of NPC xenograft tumor models in DDP combined with different treatment groups. DDP, cisplatin; G, galunisertib. $n = 5$ per group at each time point; *$p < 0.05$ versus control; #$p < 0.05$ versus the DDP + galunisertib + BEV group. The p values are shown in Table S5. (B) DDP-modified DNA immunoreactivity in the tumor areas of different treatment groups. $n = 5$ per group. (C) Representative images of DDP-positive staining in the tumor areas of different treatment groups. Scale bar, 50 μm.

that TGFB1 induced an increase in the LAMC2 levels in HNE2 and HK1 cells, thus promoting the EMT process; however, this was blocked by galunisertib and TGFB1-neutralizing antibodies (Figure 7A). These findings suggested that the expression of LAMC2 in tumor tissues might play an intermediate mediating role in the effect of galunisertib in reversing EMT in NPC cells. To determine the effect of LAMC2 on EMT and TVN in tumors, LAMC2 was knocked down in HNE2 and HK1 cells induced by small interfering RNA (siRNA) transfection, and the expression of EMT-related proteins, HIF-1α, and VEGF was analyzed by western blotting assay. After LAMC2 was silenced for 24 h, the appearance of the cells changed from long spindles to elliptic polygons or cobblestones, and they became more tightly packed (Figure 7C). Relative to the control group (si-Control, NC), the si-LAMC2 knockout group showed considerably higher E-cadherin levels but lower vimentin and N-cadherin levels (Figure 7B). Additionally, HIF-1α and VEGF levels were considerably lower in the LAMC2-knockout group relative to that in the NC (Figure 7D). These results indicated that galunisertib reversed TGFB1-induced EMT and inhibited the expression of HIF-1α and VEGF by downregulating the expression of LAMC2.

Galunisertib downregulated LAMC2 levels via the JNK/AP1 pathway

We further analyzed the mechanism by which galunisertib downregulates LAMC2 in cancer cells. The transcription of the LAMC2 gene is associated with AP1 (mostly c-Fos and c-Jun).[32] JNK is the upstream signal of AP1 and an important pathway associated with TGFB regulation. To determine whether the JNK/AP1 signaling pathway is related to the regulation of LAMC2 by galunisertib, we stimulated NPC cells using different doses of TGFB1 (0, 10, 20, and 30 ng/mL) or TGFB1 (20 ng/mL), galunisertib (8 μM), TGFB1 + galunisertib, and TGFB1 + TGFB1-neutralizing antibody (1 μg/mL) for 48 h. We conducted a western blotting assay to detect activated AP1 (phosphorylated c-Fos [p-c-Fos] and phosphorylated c-Jun [p-c-Jun]) and phosphorylated stress-activated protein kinase (SAPK)/JNK (p-SAPK/JNK). Our results showed that changes in the expression of LAMC2 matched the changes in the expression of p-SAPK/JNK, p-c-Jun, and p-c-Fos in HNE2 and HK1 cells (Figure 7E). Galunisertib and TGFB1-neutralizing antibodies suppressed TGFB1-induced JNK/AP1 signaling (Figure 7F). After the HNE2 and HK1 cells were subjected to treatment with different concentrations of JNK inhibitor (SP600125) (0, 10, 20, and 30 μM) for 48 h, the expression of LAMC2 also decreased (Figure 7G).
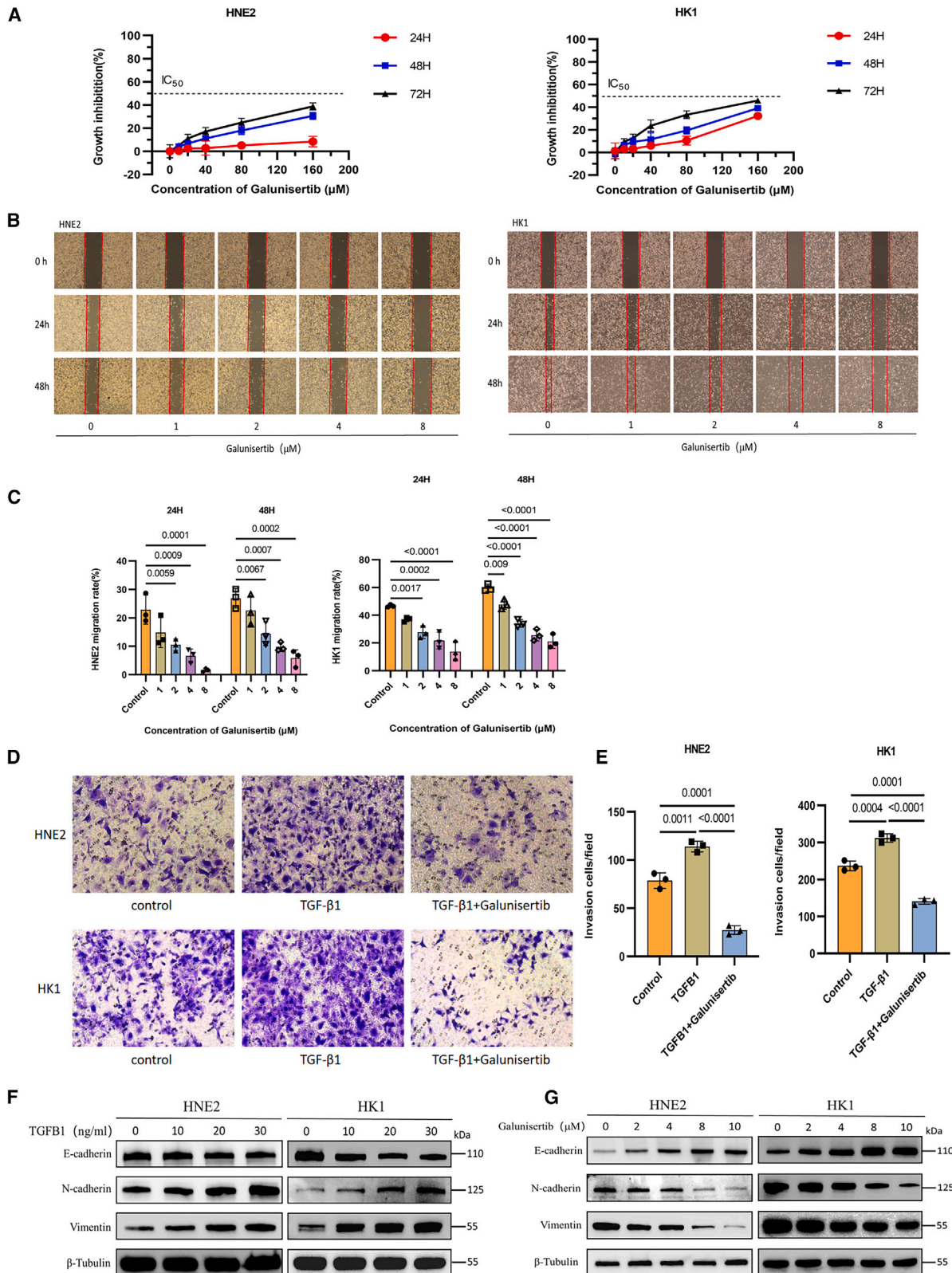
These results indicated that galunisertib can hinder the expression of LAMC2 through the JNK/AP1 pathway in NPC cells.

MRI dynamic monitoring of TVN and evaluation of the treatment response

We performed DCE-, IVIM-, and APT-MRI at different time nodes for monitoring TVN and response to treatment. The DCE-MRI parameters (K^{trans}) and the IVIM-MRI parameters (f and D^*) were measured for the whole tumor area. We found that K^{trans} of the subcutaneous PDX NPC mouse model after galunisertib monotherapy, BEV monotherapy, and galunisertib + BEV combination therapy decreased from the third day after treatment, and the combined treatment group always had a significantly lower K^{trans} value. It was notably lower in the combination treatment group relative to that in the control and monotherapy groups (Figures 8A and 8C). The f value in all treatment groups increased, but the f value of the combined treatment group was always lower, and significantly lower than that in the control group (Figure 8D). The D^* value in all treatment groups started increasing on day 3 and peaked on the 7th day. The D^* of the combination treatment group elevated more significantly and remained at a higher level than the D^* of the control and monotherapy groups on day 25. In all monotherapy groups, D^* decreased to near baseline levels after a brief increase (Figure 8E). The pattern of change in K^{trans} and f at different time nodes was similar to the overall pattern of change in histological MVD. The results of the correlation analysis indicated that K^{trans} and f were significantly positively correlated with MVD (Figures 8H and 8K), suggesting that K^{trans} and f had similar effects. They can reflect the relative changes in the number of tumor blood vessels after treatment. Also, K^{trans} was weakly correlated with PCI and collagen IV (Figures 8I and 8J). D^* was strongly correlated with the vascular normalization index but not significantly correlated with MVD (Figures 8L and 8M). These findings indicated that the IVIM parameter D^* can be used to evaluate the TVN effect and monitor the TVN time window.

The difference in APT-weighted (APTw) values among all groups before treatment was not significant. After 25 days of intervention, the APTw of galunisertib monotherapy, BEV monotherapy, and control group increased; the greatest increase was recorded in the control group, and only the galunisertib + BEV combination treatment group showed a decrease. On day 25 after treatment, APTw of the combined treatment group decreased considerably relative to that in the control and BEV monotherapy groups ($p < 0.05$) (Figures 8B and 8F). The finding of the correlation analysis indicated that APTw was notably positively correlated with the expression of the tumor proliferation marker Ki67 (Figure 8G), which suggested that the value of APTw might reflect the relative change in tumor cell proliferation activity.

After combined treatment, tumor cell proliferation activity decreased, whereas apoptosis and necrosis increased.

DISCUSSION

In the present study, we demonstrated that galunisertib can enhance the TVN effect induced by BEV, alleviate tumor hypoxia, and improve the efficacy of chemotherapy. We assessed the mechanism of action of galunisertib and found that it reversed the EMT process and downregulated the expression of VEGF and HIF-1α in NPC cells, which helped in regulating the balance of tumor angiogenesis, enhancing the TVN effect, and extending the TVN time window. We also found that the downregulation of LAMC2 strongly affected this process. Here, we described a previously undiscovered combination therapeutic strategy, a mechanism mediated by crosstalk in the tumor stroma in relation to cancer cells in anticancer treatment. Additionally, the significant correlation between multiple parameters of MRI and histopathological TVN indices and cell-proliferative activity indices revealed the feasibility of non-invasive MRI monitoring of the TVN time window and tumor therapeutic response, which provided strong support for the clinical transformation of combined treatment strategies.

Galunisertib (LY2157299) represents the oral small-molecule inhibitor of TGFB receptor I (TGFB RI) kinase. It effectively suppresses the TGFB pathway by blocking the kinase domain in TGFB RI. In this study, galunisertib monotherapy and BEV monotherapy delayed the growth of NPC tumors, but the difference in efficacy between the two treatment strategies was not significant. However, adding galunisertib significantly enhanced the antitumor effect of BEV. This matched the findings of previous studies, suggesting that the simultaneous targeting of the VEGF/VEGF-R axis and TGFB pathway can synergistically reduce tumor angiogenesis and enhance antitumor activity.[33,34] By conducting histological analysis at different treatment time points, we also dynamically evaluated the influence of different treatment schemes on the vascular histopathological features of the NPC PDX model. Our findings showed that galunisertib and BEV combined therapy promoted TVN and extended the normalization time window, and the degree of TVN was higher than that of BEV alone 25 days after treatment. Although combined therapy decreased the vascular density of NPC tumors, it promoted the maturation of the vascular structure and function of tumors.

Tumor hypoxia is a vital index for evaluating the normalization of blood vessels and also an important incentive to hinder the normalization of blood vessels. HIF-1α is regulated by tumor hypoxia. The upregulation of HIF-1α can promote the adaptation and survival of tumors under hypoxic conditions by inducing the transcription of

---

Figure 6. Effects of galunisertib on the proliferation, migration, invasion, and EMT process in NPC cells

(A) CCK8 assay showed the effect of galunisertib on the proliferation of HNE2 and HK1 cells. (B) Wound-healing assay showed that galunisertib inhibited the migration of HNE2 and HK1 cells; magnification, 40×. (C) Quantification of the results of the wound-healing assay. $n = 3$ per group. (D) Transwell assay showed that galunisertib inhibited the invasion of HNE2 and HK1 cells upregulated by TGFB1; magnification, 200×. (E) Quantification of the results of the Transwell assay. $n = 3$ per group. (F) Western blotting showed that TGFB1 promoted the EMT process in HNE2 and HK1 cells. (G) Results of the western blotting assay showed that galunisertib hindered the EMT process in HNE2 and HK1 cells. In (F) and (G), β-tubulin served as the loading control. Quantitative analysis of western blotting is shown in Figure S3.
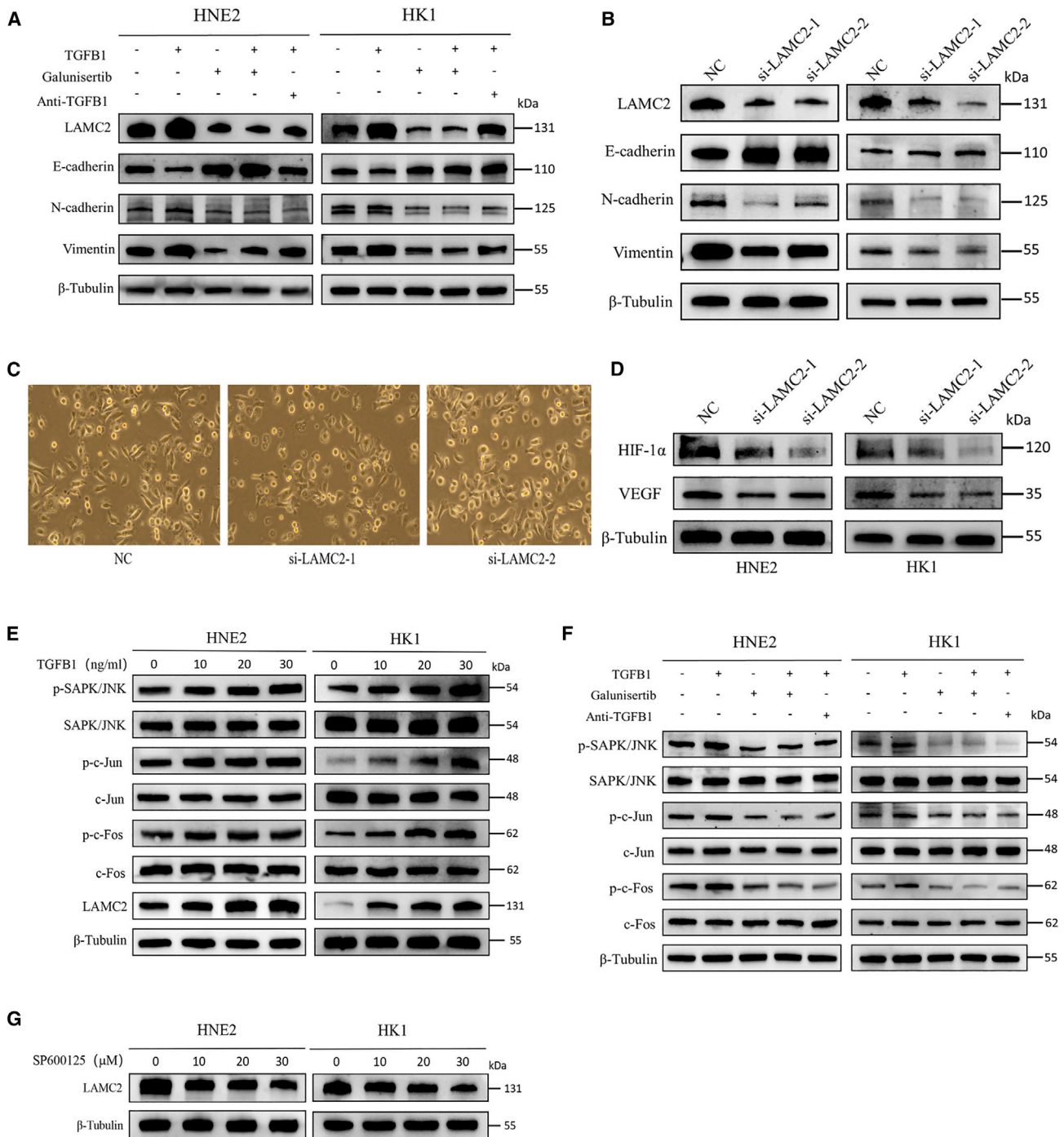
Figure 7. Galunisertib reversed the EMT process and inhibited HIF-1α and VEGF levels by downregulating LAMC2

(A) Western blotting assay confirmed the effects of galunisertib and anti-TGFB1 (1 mg/mL, 521707, BioLegend) on the inhibition of the TGFB1-induced EMT process and expression of LAMC2. (B) Western blotting assay showed that the knockout of the LAMC2 protein inhibited the EMT process. (C) EMT-like morphological changes were observed in HK1 cells after siRNA interference with LAMC2; magnification, 200×. (D) Western blotting assay showed that the knockout of the LAMC2 protein inhibited the expression of HIF-1α and VEGF. (E) Western blotting assay showed that TGFB1 upregulated LAMC2 by promoting the JNK/AP1 signaling pathway. (F) Western blotting assay showed that galunisertib and anti-TGFB1 inhibited TGFB1-induced activation of the JNK/AP1 pathway. (G) Western blotting assay indicated that SP600125 downregulated the expression of LAMC2 by inhibiting the JNK signal. In (A), (B), and (D)–(G), β-tubulin served as the loading control. Quantitative analysis of western blotting is shown in Figures S4 and S5.
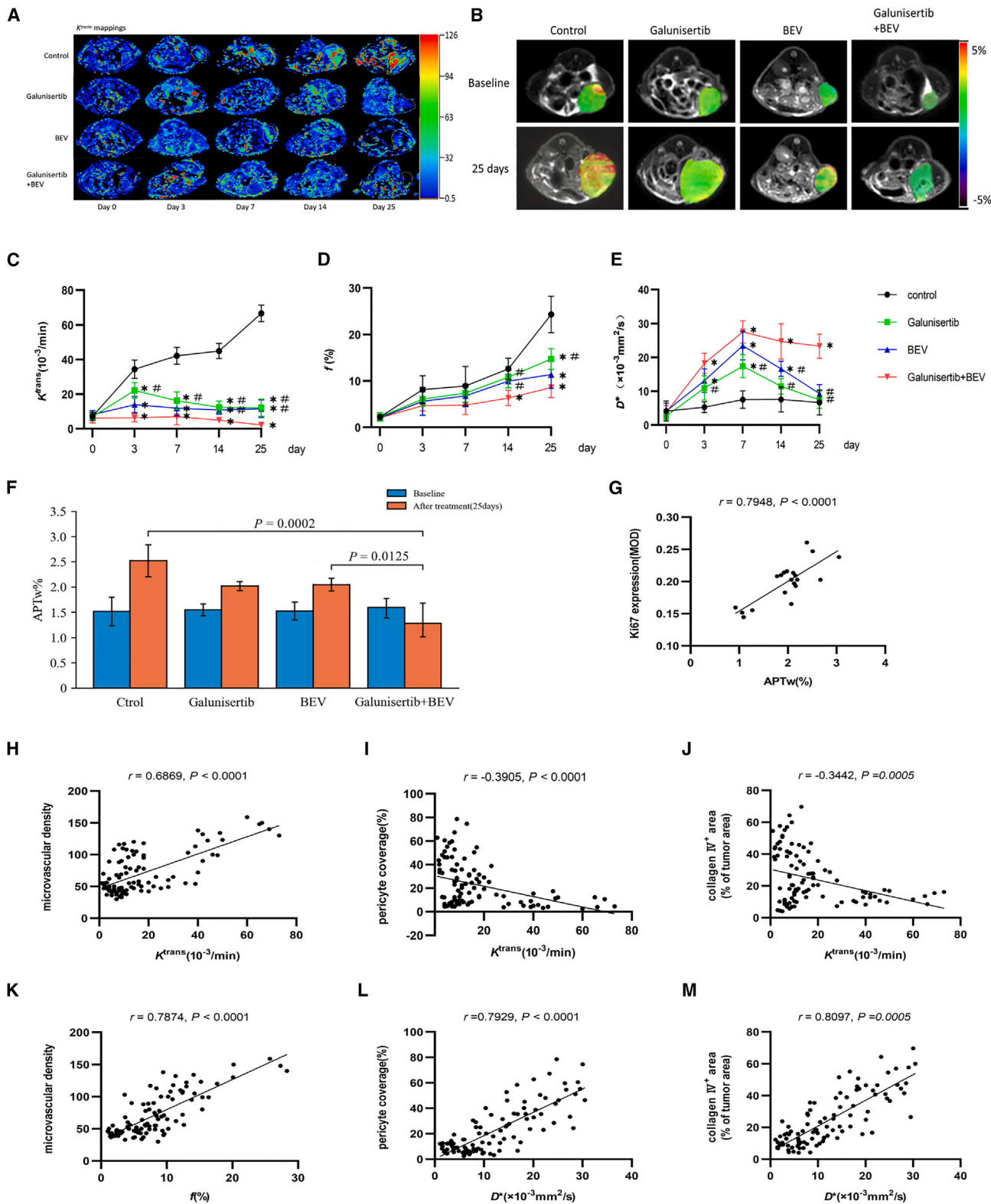
multiple downstream genes, including genes that stimulate angiogenesis and the switching of cell metabolism from oxidative processes to anaerobic respiration.[35] These events together facilitate an increase in tumor grade, chemotherapy, and resistance to radiotherapy, thus leading to poor clinical outcomes. Our findings showed that the HIF-1α level was notably lower in the combination treatment group than in the control and BEV groups, indicating that the enhanced TVN effect significantly improved tumor hypoxia. The HIF-1α level in tumors was lower in the galunisertib monotherapy group relative to that in the BEV monotherapy group, although differences in the indices related to tumor microvascular density and vascular function were not significant between the two groups. Our findings suggested that galunisertib might directly regulate HIF-1α levels. We also found that galunisertib inhibited TGFB1-mediated VEGF and HIF-1α expression in NPC cells at the cellular level. These results elucidated the mechanism by which galunisertib promoted the antitumor effect of BEV. On the one hand, by inhibiting the secretion of VEGF, galunisertib can cooperate with BEV to inhibit the VEGF/VEGF-R axis and help regulate the balance between pro-angiogenic factors and anti-angiogenic factors. On the other hand, when the non-VEGF/VEGF-R alternative pathway was activated, and the above balance was disrupted, galunisertib alleviated the hypoxia response mechanism in the TME by decreasing the HIF-1α level and further inhibiting the expression of pro-angiogenic factors, which helped in re-establishing the balance of angiogenesis regulation. These changes extended the TVN effect. Similarly, tumor hyperproliferation and invasion were inhibited correspondingly, and tumor apoptosis was promoted due to the decrease in HIF-1α level. These findings were similar to our experimental results.

Some studies have suggested that the remodeling effect induced by the TME generated by TVN can improve the sensitivity of tumors to chemotherapeutic drugs and the delivery rate of these drugs to tumors.[35] Administering chemotherapy during the time window can promote the distribution and aggregation of chemotherapeutic drugs in the tumor, which can significantly enhance the efficacy of treatment.[36] This hypothesis matched our findings. Low-dose DDP (1 mg/kg) did not have a significant antitumor effect on NPC xenografted tumors, whereas galunisertib improved the efficacy of low-dose DDP by improving vascular function and anoxia in the TME. Compared to monotherapy, galunisertib + BEV combined therapy greatly enhanced low-dose DDP delivery, resulting in a more significant tumor-suppressive effect. Additionally, systemic toxicity of the chemotherapeutic agents was not significant.

The EMT process is associated with malignant phenotype and angiogenesis of tumors.[37] Our results indicated that galunisertib can inhibit tumor migration and invasion by reversing the EMT process in NPC

cells. Some studies have found that EMT can increase the resistance of cancer cells to chemotherapy.[38] Similar findings were reported in another study in which genetically engineered mice were used to construct the pancreatic ductal adenocarcinoma model.[39] Subsequent studies on the mechanism of action showed that EMT inhibited the expression of drug transporters and protein concentrate. Thus, targeting EMT might be an effective strategy for enhancing chemotherapeutic effects or the efficacy of other treatment strategies. This might be another reason why galunisertib monotherapy and galunisertib + BEV combined therapy enhanced the efficacy of DDP chemotherapy in the present study.

We also discovered that the expression of LAMC2 decreased after treatment with galunisertib. LAMC2 encodes the laminin γ chain in laminin −332 and is related to the invasion and metastasis of multiple cancer cell lines.[40,41] Gene enrichment analysis of pancreatic cancer based on public databases in another study showed that LAMC2 is significantly enriched in the transcription profiles of squamous subtypes, TGFB-related transcription profiles, and hypoxia and MAPK pathways.[42] Our results demonstrated that TGFB1 was positively related to LAMC2 expression in NPC clinical specimens. LAMC2 expression was upregulated after TGFB1 stimulation, which was inhibited by galunisertib and TGFB1-neutralizing antibodies. These results suggested that LAMC2 might be a potential target of NPC cells affected by galunisertib. After LAMC2 was silenced by siRNA, the EMT process in NPC cells was inhibited, which was consistent with the effect of galunisertib. LAMC2 was also found to be associated with tumor angiogenesis. LAMC2 silencing can inhibit the angiogenesis of bile duct carcinoma by inactivating epidermal growth factor receptor signaling pathways.[43] These findings were similar to those arising from our results. After LAMC2 was knocked down via siRNA, the expression of VEGF and HIF-1α decreased, which was consistent with the effect of galunisertib. The findings of these experiments demonstrated that an increase in the LAMC2 levels was significantly correlated with the tumor EMT process and tumor angiogenesis, which can predict poor prognosis in NPC patients. Therefore, LAMC2 might be an efficient therapeutic target for treating NPC.

Monitoring the progression of TVN can help in determining the window period of TVN and formulating other combined treatment plans. Among the available quantitative MRI methods, DCE, IVIM, and APT imaging can be performed to elucidate the microscopic structure and microvascular system in cancer lesions.[44,45] DCE-MRI is a functional imaging technique that is used in clinical studies for evaluating the effect of anti-angiogenic drugs.[46] The MRI parameter K^{trans} is a key factor that reflects the volume transfer coefficient between plasma and the extravascular space of contrast media.[47] A high K^{trans} value

Figure 8. MRI dynamic monitoring of the TVN process and evaluation of the response to treatment

(A) Representative K^{trans} images at different time points in different treatment groups. (B) Representative APTw images were obtained 25 days after intervention for different treatment groups. Comparison of K^{trans} (C), f (D), and D^* (E) at different times. Comparison of APTw at different times (F). Correlations between APTw and Ki67 (G), K^{trans} and MVD (H), K^{trans} and PCI (I), K^{trans} and collagen IV (J), f and MVD (K), D^* and PCI (L), and D^* and collagen IV (M) are shown. In (C)–(E), *$p < 0.05$ versus control, #$p < 0.05$ versus the galunisertib + BEV group. $n = 5$ per group at each time point. The p values are shown in Table S6.

indicates active tumor vascular growth, high vascular permeability, and high malignancy.[48] However, its application is hindered by adverse reactions caused by contrast agents, such as allergic reactions, contrast-induced nephropathy, extravasation, and nephrogenic systemic fibrosis.[49] IVIM-MRI imaging reflects the diffusion and perfusion of water molecules. As reported in other studies,[50–53] we found that K^{trans} and the f value were significantly positively correlated with MVD, which together reflected tumor angiogenesis. A significant correlation was found between D^{*} and PCI or collagen IV, as reported in another study,[30] and this finding indicated that the increase in D^{*} can reflect the improvement in tumor vascular function. However, the results of another study showed that D^{*} was poorly related to pathological factors, which contradicted our finding.[50] The difference between the results of that study and ours might be associated with the b-value parameter setting or the postprocessing software used. APT imaging is a novel MRI technology used for evaluating the endogenous levels of mobile proteins along with peptides in tissues through amide proton saturation in peptide bonds. APT can be used to evaluate efficacy in glioma and rectal and breast cancers.[54–56] The intensity of the APT signal is affected by the protein level and cell density of tumor tissue.[57] We found that the combined treatment group showed apoptotic features, which explained the reason for the reduction in the intensity of the APT signal. The APTw value showed a significantly positive relationship with the tumor proliferation marker Ki67, which matched the results of previous studies on breast cancer and rectal cancer.[58,59] These results indicated that IVIM-MRI can replace DCE-MRI in evaluating tumor angiogenesis and can be used repeatedly to assess treatment response within a short period, irrespective of the adverse effects of contrast agents. APTw can reflect tumor cell proliferation activity. Thus, MRI multi-parameter scanning can be performed to assess histological changes in multiple dimensions, which can facilitate early and accurate assessment of the response to anti-angiogenic therapy and guide the application of combination therapy.

This study has some limitations. First of all, TVN involves multiple signaling pathways, and this study did not specifically elucidate how the downregulation of LAMC2 by dual-targeted therapy further regulates TVN. In the future, it will be necessary to further study the specific molecular mechanism of LAMC2 regulating tumor angiogenesis and vascular normalization. In addition, this study only focused on the correlation between K^{trans}, D^{*}, and f and TVN indicators. In subsequent studies, we can use more comprehensive MRI parameters and more complex pharmacokinetic models to explore the superiority of multi-parameter MRI monitoring of the TVN process. In conclusion, we showed that galunisertib can enhance the TVN effect induced by BEV, which can significantly improve the delivery rate of chemotherapeutic drugs and enhance the antitumor effect of chemotherapy. Hence, the application of galunisertib is a new treatment strategy for enhancing the NPC TVN effect. We initially found that LAMC2 regulated by the JNK/AP1 signaling pathway might be a key regulator for the regulation of TVN by galunisertib. Finally, multi-parameter MRI imaging can be used for non-invasive and real-time monitoring of tumor anti-angiogenesis therapeutic response. This technique can substitute the pathological index for monitoring the time window of TVN and help clinicians to make decisions related to clinical treatment.

MATERIALS AND METHODS

Bioinformatics analysis
We studied the differential expression of the TGFB1 and LAMC2 genes in pan-cancer versus adjacent non-carcinoma tissues in TCGA (https://tcga-data.nci.nih.gov/tcga/) on the TIMER website (http://timer.cistrome.org/). We plotted Kaplan-Meier survival curves to analyze 566 samples of RNA-sequencing TPM from HNSCC in TCGA, using the "survival" package. We also examined the relationship of TGFB1/LAMC2 with clinical factors, containing age, sex, TNM stage, and tumor grade. We conducted the Mann-Whitney U test to analyze the relationship between the expression of the TGFB1/LAMC2 genes and clinical information. For processing and analyzing the TCGA-HNSCC data, we used R software (version 3.6).

Clinical samples and cell lines
All clinical NPC tissue specimens were gathered at the Affiliated Hospital of Guizhou Medical University (Guiyang, China). Human NPC HNE2 cells were provided by the Cancer Institute of Xiangya Hospital, Central South University (Changsha, China). Human NPC HK1 cells were provided by Guangzhou Jennio Biotechnology (Guangzhou, China). Both cell lines were cultivated in RPMI-1640 (C11875500BT, Gibco) containing 10% fetal bovine serum (FBS: F8318, Sigma) and 1% penicillin/streptomycin (C0222, Beyotime) at 37°C with 5% CO_2.

Animal model and study design
Healthy female BALB/c mice (6–8 weeks old, 18–20 g) were selected as the model animals for xenograft tumors of NPC. Nasopharyngeal low differentiated squamous cell carcinoma cell line HNE2, with high malignant degree and easy metastasis, was selected as the inoculation cell line for NPC PDX models. A suspension of HNE2 cells (200 μL, 4×10^{7} cells) was implanted subcutaneously in the left inguinal region of the mice. After the tumor developed in the first-generation NPC PDX models, the tumor tissue was collected and sliced into small pieces (about 3 mm in diameter). Small pieces of tumor tissues were then implanted subcutaneously into the left groin area of the mice with a bone-marrow puncture needle to establish the second-generation tumor transplantation model. Using this *in vivo* passage method, we obtained NPC PDX models with a stable phenotype between individuals. The short diameter (*a*) and the long diameter (*b*) of the tumor were determined with a digital caliper at an interval of 2 days, whereas the tumor volume (*V*) was monitored using the following equation for 25 consecutive days.[30] The weight of the mice was measured, and severe adverse reactions were monitored.

$$V = \frac{a^2 \times b}{2}.$$

Animals that had a hard lump with a long diameter greater than 6 mm were considered to be successful models for this study. In total, 125 PDX models were established using the third-generation transplanted tumor models. Group administration intervention was initiated after successful modeling. We randomly placed 100 tumor-bearing mice into four groups (n = 25 mice per group), including the control, galunisertib, BEV, and galunisertib + BEV groups. The endpoint of treatment was determined by severe weight loss (20% weight loss) in the tumor-bearing mice.[60] The study protocol is schematically presented in Figure 1. MRI examinations and histopathological analysis were performed at different time periods (0, 3, 7, 14, and 25 days). The group 25 days after treatment was used as the treatment observation group to evaluate the treatment effect. For evaluating the efficacy of the chemotherapeutic drug, another 25 NPC PDX models were randomly placed in five drug-treatment groups (n = 5 mice per group) (placebo, DDP, DDP + galunisertib, DDP + BEV, and DDP + galunisertib + BEV). Tumor samples were gathered 24 h after the last DDP administration to evaluate the delivery efficiency of DDP and assess the therapeutic effect. Galunisertib (HY-13226, MCE; 75 mg/kg, administered twice a day) was dissolved in 1% carboxylmethyl cellulose sodium (CMC-Na; HY-Y0703, MCE) as a drug carrier and administered intragastrically.[60] BEV (1110030973, Bevagen; 5 mg/kg, administered twice a week) and DDP (HY-17394, MCE; 1 mg/kg, administered every 4 days) were diluted with 0.9% normal saline and injected intraperitoneally.[30,61] The mice in the control group were administered 1% CMC-Na/0.9% normal saline.

Immunohistochemistry and immunofluorescence

Tumor tissue samples were collected from mouse transplanted tumor models of different drug-treatment groups 1 day before treatment (0 days at baseline) and 3, 7, 14, and 25 days after treatment. Using 4% paraformaldehyde, the tumor tissues were first fixed, then embedded in paraffin and sliced to form continuous sections (about 4 mm thick). These slices were dewaxed, rehydrated, and incubated with 3% H_2O_2 to block endogenous peroxidase. 10% goat serum was then added to seal the sections, which were then incubated overnight with primary antibodies at 4°C. Horseradish peroxidase (HRP)-conjugated goat anti-mouse (GB23301) or goat anti-rabbit (GB23303, Servicebio; 1:200) secondary antibodies were used for immunohistochemistry. In immunofluorescence staining, CY3-labeled goat anti-rabbit (GB21303) or Alexa Fluor 488-labeled goat anti-mouse (GB25301, Servicebio; 1:400) fluorescence secondary antibodies were used. The primary antibodies used included Ki67 (9449, CST; 1:80), CD31 (GB11063-2, Servicebio; 1:200), collagen IV (bs-4595R, Bioss; 1:100), α-smooth muscle actin (α-SMA; GB111364, Servicebio; 1:200), TGFB1 (ab215715, Abcam; 1:50), LAMC2 (ab210959, Abcam; 1:50), HIF-1α (36169T, CST; 1:80), and DDP-modified DNA antibody (CP9/19; NBP2–50165, Novus; 1:50). The TUNEL assay was performed using a dye (G1501, Servicebio) following specific protocols. Images of all stained sections were obtained using an upright optical microscope (Nikon Eclipse C1, Nikon) or a confocal laser scanning microscope (TCS SP8, Leica). Image-Pro Plus 6.0 software (Media Cybernetics) was adopted for selecting three typical visual fields for each section to conduct the analysis. MVD was quantified by the "hot spot" approach.[62] First, the area with the highest microvascular density around the three cancer nests, i.e., the vascular hot spot, was observed and identified under a 100-fold low-power microscope to determine the MVD calculation area. The number of microvessels was then counted manually under a 200-fold visual field, and the MVD value was calculated using the average number recorded in the three hot spots. One countable vessel included a microvascular endothelium or a cluster of endothelial cells with positive staining that was isolated from the surrounding cancer cells and microvessels under the microscope.[62] Vessels with smooth muscle walls with red blood cells in the lumen were not counted.[63] PCI was determined by a positive α-SMA-to-CD31 staining ratio.[30] HIF-1α was quantified by measuring fluorescence intensity.[64] The quantification of Ki67 or DDP-modified DNA was evaluated by mean optical density.[65]

Hematoxylin and eosin staining

To evaluate the systemic toxicity of the drug in mice, their liver, spleen, and kidney tissues were fixed with 4% paraformaldehyde, embedded in paraffin, and sliced to obtain continuous sections (about 4 mm thick) 25 days after treatment. The sections were stained with hematoxylin after dewaxing and rehydration for 5 min and then rinsed with running water. Next, they were differentiated using a differentiating solution, washed with running water, treated with an anti-blue solution, and washed again with running water. After the sections were dehydrated for 5 min with 85% and 95% alcohol, they were stained for another 5 min using an eosin dye solution. The sections were then dehydrated, sealed, and observed under a 100× optical microscope.

Western blotting assay

The RIPA lysate (p0013B, Solarbio) containing protease/phosphatase inhibitor (HY-K0022, MCE) was used for extracting total proteins from tissues and cells following the instructions of the manufacturer. The protein content was determined using the BCA Protein Assay Kit (PC0020, Solarbio); 10% separation gel and 5% concentrated gel were used for the assay. Concentrated glue and separated glue were prepared following the instructions provided with the acrylamide dye-free glue kit (1610183, Bio-Rad). The protein content of each sample was about 20 μg. After electrophoresis, the proteins were transferred onto polyvinylidene fluoride membranes, which were later sealed with 5% defatted milk containing Tris-buffered saline and Tween 20 for 45 min. Next, the membranes were subjected to incubation with primary antibodies at 4°C overnight (Table S2). β-Tubulin was applied as an internal reference. The membranes were then incubated with secondary antibodies for 1 h under ambient temperature. The secondary antibodies used included monoclonal antibody HRP-labeled immunoglobulin G goat anti-rabbit (RS0001, Immunoway; 1:10,000) or goat anti-mouse (RS0002, Immunoway; 1:10,000) antibodies. The membrane was visualized using an enhanced chemiluminescence solution.

Cell Counting Kit-8 assay

For assessment of the effect of galunisertib on the activity of NPC cells, HNE2 and HK1 cells (3×10^4/mL) were seeded in 96-well plates

(100 μL/well) and incubated overnight at 37°C. Next, 0–160 μM galunisertib was supplemented to treat cells for 24, 48, and 72 h. DMSO was used as the negative control. The prepared CCK8 reaction solution (CCK8 buffer/serum-free medium, 1:9) was added to every well, and the mixture was incubated at 37°C in darkness for 2 h. The 96-well plate was placed in an enzyme-labeled instrument to measure absorbance at 450 nm. Cell survival was calculated using the following equation: cell survival rate (%) = [drug group − blank group]/[control group − blank group] × 100%. The absorbance of the blank group included the absorbance of the well containing the medium and the CCK8 solution without cells. GraphPad Prism 8.0 software (GraphPad, USA) was applied to plot cell-growth curves.

siRNA-mediated knockdown

The HNE2 and HK1 cells were seeded in 12-well culture plates and incubated with 5% CO_2 at 37°C. Cells in the logarithmic growth stage were transfected when the degree of cell fusion reached 50%–60%. LAMC2-siRNA constructs were purchased from RiboBio Biotechnology (Guangzhou, China). Following specific protocols, we used the riboFECTTMCP reagent (SIGS0006927-4, RiboBio) for transfecting siRNA targeting LAMC2 (siLAMC2-1: 5′-GTC AAA GCC TGT CCT TTG A-3′; siLAMC2-2: 5′-TCG GGA ACT TCA CAG ACA A-3′). At 24 h after transfection, we extracted total tumor cellular proteins and performed a western blotting assay to evaluate the downregulation of LAMC2 in cancer cells.

Wound-healing and Matrigel cell invasion assays

Cells were first cultured in 6-well plates (5×10^5 cells/well) filled with RPMI-1640 medium including 10% FBS at 37°C with 5% CO_2 in an incubator until cell fusion reached 90%. Next, the bottom of the 6-well plate was scratched vertically using the tip of a sterile pipette. The original medium was then aspirated, and free cells were removed by rinsing with PBS. The samples were diluted to the desired dose in serum-free RPMI-1640 medium, after which the drug was added for treating the cells for 24 h and 48 h at 37°C with 5% CO_2. The negative control group was added with 1/1,000 of DMSO. All cells were observed under an optical microscope, and images were acquired after 0, 24, and 48 h.

Matrigel (3432-010-01, R&D Systems) was defrosted overnight at 4°C in advance. Next, 60 μL of Matrigel was precoated on a membrane in the top 24 wells in the Transwell chamber (0.8 μm pore size; Corning) in line with the instructions of the manufacturer. The Transwell chamber covered with Matrigel was incubated at 37°C with 5% CO_2 for at least 1 h, then cell suspensions prepared in 200 μL of serum-free medium (3×10^5/mL) were added to the top chamber. In the bottom chamber, 600 μL of RPMI-1640 medium, containing 20% FBS, was supplemented. After incubation for 24 h at 37°C under 5% CO_2, a cotton swab was applied to gently rub the inner surface of the chamber to remove cells that did not migrate onto the back. Next, 4% paraformaldehyde was added for 30 min to fix the cells at room temperature. The cells were then stained using 0.5% crystal violet solution for 20 min under ambient temperature. Finally, images of invading cells were acquired with an optical microscope.

MRI scanning and data postprocessing

The MRI experiment was carried out with a 3.0-T scanner (Elition X, Philips Healthcare, Best, the Netherlands) equipped with an eight-channel mouse coil (HC607P, Hezi Medical Technology, Wuxi, China). MRI scanning was performed 1 day before treatment (0 days at baseline) and 3, 7, 14, and 25 days after treatment. The scanning sequence included the following: T1-weighted imaging (T1WI), T2-weighted imaging (T2WI), amide proton transfer-weighted imaging (APTWI), and IVIM along with DCE. The parameters were described as follows. (1) T1WI: turbo spin echo (TSE); echo time (TE) = 20 ms; repetition time (TR) = 2,000 ms; inversion recovery time (TI) = 800 ms; field of view (FOV) = 60×60 mm^2; matrix = 150×150; slice thickness = 1 mm. (2) T2WI: TSE Multivane; TE = 137 ms; TR = 2,500 ms; FOV = 60×60 mm^2; matrix = 150×150; slice thickness = 1 mm. (3) APT-MRI: Z-spectrum with maximum cross-section of the tumor was collected to construct an asymmetrical magnetization transfer ratio (MTR_{asym}) chart. Two-dimensional TSE: TE = 15 ms; TR = 4,933 ms; FOV = 60×60 mm^2; matrix = 120×120; slice thickness = 4 mm; number of excitations (NEX) = 2 times; saturation frequency: +3.5 ppm (acquired three times with each acquisition window shifted by 0.4 ms), −3.5 ppm, ±2.7 ppm, ±4.3 ppm, and −1,560.0 ppm. Data collection time was 3 min 18 s. (4) IVIM-MRI: TSE diffusion-weighted imaging; TE = 125 ms; TR = 2,000 ms; FOV = 60×60 mm^2; matrix = 64×64; slice thickness = 1 mm; 10 b values: 0, 10, 20, 30, 40, 80, 150, 300, 500, and 800 s/mm^2. The number of signal averages (NSA) for the last two b values was 6, while the NSA of the other b values was 3. (5) DCE-MRI: before scanning, a 26-gauge intravenous indwelling needle was used to puncture the tail vein of tumor-bearing mice and establish intravenous drug-delivery channels. Scanning procedure: first, T2WI scanning was performed as the localizer, then two T1 mapping scans were performed based on T2WI using the double flip angle (FA) technique. Scanning parameters of T1 mapping: turbo field echo (TFE); TE = 4.2 ms; TR = 8.3 ms; FOV = 60×60 mm^2; matrix = 150×150; slice thickness = 1.5 mm; first sequence FA: 5°; second sequence FA: 15°. DCE-MRI scanning was then carried out, and the main imaging parameters were the same with the T1 mapping sequences, except that the FA was 20°. In total, 80 dynamics of DCE-MRI were scanned, each dynamic was 8.8 s, and total acquisition time was 11 min 49 s. Gadopentetic acid meglumine solution (H19991127, Xudong Hepu Pharmaceutical, Shanghai, China) was manually injected through the caudal vein at DCE-MRI scan dynamic 5. The concentration of the contrast agent was 100 mmol/kg.

The APTw images were reconstructed using the built-in APT image reconstruction algorithm. Region of interest (ROI) was plotted based on the T1WI and T2WI images, including the entire tumor region, and the APT-weighted values of each ROI were recorded. The specific steps were as follows. First, the three images with saturation frequencies of +3.5 ppm were calculated by the Dixon postprocessing algorithm to obtain magnetic field inhomogeneity image B0. Next, the images acquired with different saturation frequencies were interpolated to correct the frequencies and the errors caused by the inhomogeneity of the B0 field. Images obtained at saturation frequency

−1,560 ppm are generally considered to have no magnetization transfer effect, and thus the image can be denoted as S_0. If the image obtained at a different saturation frequency is denoted as S_{sat}, $1 - S_{sat}/S_0$ is defined as the magnetization transfer ratio (MTR). The APT-weighted value APTw was then defined as the MTR_{asym} (3.5 ppm) = $[S_{sat} (-3.5\ ppm) - S_{sat} (+3.5\ ppm)]/S_0$.[66] The IVIM image was analyzed using MITK-Diffusion software (German Cancer Research Center). The IVIM parameters were evaluated by the biexponential model, and the corresponding parameter maps were generated.[67] The IVIM parameters included the slow apparent diffusion coefficient (ADC) (D), fast ADC (D^*), and the fraction of the fast ADC (f). Among these, D and D^* are true and pseudo diffusion coefficients, respectively; f indicates the perfusion fraction. The DCE-MRI images were processed by IntelliSpace Portal 9.0 software (ISP, Philips). The quantitative parameter volume transfer constant (K^{trans}) was calculated using the Extended Tofts-Ketty pharmacokinetic model, and a map was generated. In each parameter diagram, the maximum layer of the tumor was selected to manually draw the ROI of mice, and the average value of all voxels in the ROI was considered to be the average value of the ROI.[30]

Statistical analysis

We used GraphPad Prism 8.0 and SPSS 21.0 (IBM, USA) to process experimental data. All data are presented as the mean ± SD. The normality of the data was assessed by the Shapiro-Wilk test. The two groups of samples were compared by Student's t tests. Multiple groups of samples were compared by one-way ANOVA and Tukey's test. The correlation between MRI parameters and pathological parameters was determined by Pearson's correlation analysis; $0.7 < |r| < 1.0$, $0.4 < |r| < 0.7$, and $0.2 < |r| < 0.4$ indicated strong, moderate, and weak correlations, respectively. Survival comparison was analyzed by the log-rank test. All results were regarded to be statistically significant at $p < 0.05$.

Study approval

All patients provided written informed consent before sample collection. All human biopsy sample studies were carried out in accordance with the principles of the Declaration of Helsinki and were approved by the Human Research Ethics Committee of the Affiliated Hospital of Guizhou Medical University.

All animal experiments were approved by the Animal Care Welfare Committee of Guizhou Medical University (Protocol 2304152) and conducted in accordance with the National Institutes of Health Guidelines for the Care and Use of Laboratory Animals (National Academies Press, 2011).

DATA AND CODE AVAILABILITY

All data involved in the work can be obtained from Prof. Bo Gao (gygb2004@gmc.edu.cn) upon reasonable request.

SUPPLEMENTAL INFORMATION

Supplemental information can be found online at https://doi.org/10.1016/j.omton.2024.200858.

AUTHOR CONTRIBUTIONS

J.Y., S.Z., and B.G. designed the research. J.Y., Z.L., X.L., and Q.H. performed the experiments. J.L. and P.W. provided the necessary reagents and techniques for this study and reviewed the manuscript. J.Y., X.D., and P.C. were involved in the drafting of the paper and the analysis and interpretation of data. B.G. contributed to the idea and key revisions of the manuscript as well as analysis and interpretation of data, and approved the final version of the submitted manuscript. All authors read and approved the final manuscript.

DECLARATION OF INTERESTS

The authors declare no competing interests.

REFERENCES

1. Chan, K.C.A., Woo, J.K.S., King, A., Zee, B.C.Y., Lam, W.K.J., Chan, S.L., Chu, S.W.I., Mak, C., Tse, I.O.L., Leung, S.Y.M., et al. (2017). Analysis of Plasma Epstein-Barr Virus DNA to Screen for Nasopharyngeal Cancer. N. Engl. J. Med. 377, 513–522.

2. Mai, H.Q., Chen, Q.Y., Chen, D., Hu, C., Yang, K., Wen, J., Li, J., Shi, Y.R., Jin, F., Xu, R., et al. (2021). Toripalimab or placebo plus chemotherapy as first-line treatment in advanced nasopharyngeal carcinoma: a multicenter randomized phase 3 trial. Nat. Med. 27, 1536–1543.

3. Masterson, L., Howard, J., Gonzalez-Cruz, J., Jackson, C., Barnett, C., Overton, L., Liu, H., Ladwa, R., Simpson, F., McGrath, M., et al. (2020). Immune checkpoint inhibitors in advanced nasopharyngeal carcinoma: Beyond an era of chemoradiation? Int. J. Cancer 146, 2305–2314.

4. Gong, X., Wang, L., Wu, W., Li, Y., Long, J., Chen, X., Luo, X., He, Q., Bi, T., Li, Z., et al. (2022). The Treatment Combining Antiangiogenesis with Chemoradiotherapy Impinges on the Peripheral Circulation Vascular Endothelial Cells and Therapeutic Effect in the Patients with Locally Advanced Nasopharyngeal Carcinoma. BioMed Res. Int. 2022, 1787854.

5. Zhou, T., Yang, Y., Ma, S., Lin, L., Zhou, T., Zhang, C., Ding, X., Wang, R., Feng, G., Chen, Y., et al. (2021). Bevacizumab versus placebo in combination with paclitaxel and carboplatin as first-line treatment for recurrent or metastatic nasopharyngeal carcinoma: a multicentre, randomised, open-label, phase II trial. ESMO Open 6, 100313.

6. Liu, S., Wu, F., Zhang, Y., Qin, R., Zhu, N., Li, Y., Wang, M., Zeng, Q., Xie, D., Li, Y., et al. (2020). Apatinib Combined With Radiotherapy Enhances Antitumor Effects in an In Vivo Nasopharyngeal Carcinoma Model. Cancer Control 27, 1073274820922553.

7. Chelvanambi, M., Fecek, R.J., Taylor, J.L., and Storkus, W.J. (2021). STING agonist-based treatment promotes vascular normalization and tertiary lymphoid structure

formation in the therapeutic melanoma microenvironment. J. Immunother. Cancer 9, e001906.

8. Shigeta, K., Datta, M., Hato, T., Kitahara, S., Chen, I.X., Matsui, A., Kikuchi, H., Mamessier, E., Aoki, S., Ramjiawan, R.R., et al. (2020). Dual Programmed Death Receptor-1 and Vascular Endothelial Growth Factor Receptor-2 Blockade Promotes Vascular Normalization and Enhances Antitumor Immune Responses in Hepatocellular Carcinoma. Hepatology 71, 1247–1261.

9. Luo, X., Zou, W., Wei, Z., Yu, S., Zhao, Y., Wu, Y., Wang, A., and Lu, Y. (2022). Inducing vascular normalization: A promising strategy for immunotherapy. Int. Immunopharmacol. 112, 109167.

10. Gohongi, T., Fukumura, D., Boucher, Y., Yun, C.O., Soff, G.A., Compton, C., Todoroki, T., and Jain, R.K. (1999). Tumor-host interactions in the gallbladder suppress distal angiogenesis and tumor growth: involvement of transforming growth factor beta1. Nat. Med. 5, 1203–1208.

11. Shi, X., Yang, J., Deng, S., Xu, H., Wu, D., Zeng, Q., Wang, S., Hu, T., Wu, F., and Zhou, H. (2022). TGFB signaling in the tumor metabolic microenvironment and targeted therapies. J. Hematol. Oncol. 15, 135.

12. Trivedi, T., Pagnotti, G.M., Guise, T.A., and Mohammad, K.S. (2021). The Role of TGFB in Bone Metastases. Biomolecules 11, 1643.

13. Peng, D., Fu, M., Wang, M., Wei, Y., and Wei, X. (2022). Targeting TGFB signal transduction for fibrosis and cancer therapy. Mol. Cancer 21, 104.

14. Acharya, B., Miah, S., and Frett, B. (2022). Targeting TGFB: triumphs and challenges. Future Med. Chem. 14, 455–458.

15. Lan, Y., Moustafa, M., Knoll, M., Xu, C., Furkel, J., Lazorchak, A., Yeung, T.L., Hasheminasab, S.M., Jenkins, M.H., Meister, S., et al. (2021). Simultaneous targeting of TGFB/PD-L1 synergizes with radiotherapy by reprogramming the tumor microenvironment to overcome immune evasion. Cancer Cell 39, 1388–1403.e10.

16. Chen, Z., Chen, Y., Li, Y., Lian, W., Zheng, K., Zhang, Y., Zhang, Y., Lin, C., Liu, C., Sun, F., et al. (2021). Prrx1 promotes stemness and angiogenesis via activating TGFB/smad pathway and upregulating proangiogenic factors in glioma. Cell Death Dis. 12, 615.

17. Zhang, F., Lee, J., Lu, S., Pettaway, C.A., and Dong, Z. (2005). Blockade of transforming growth factor-beta signaling suppresses progression of androgen-independent human prostate cancer in nude mice. Clin. Cancer Res. 11, 4512–4520.

18. Komuro, A., Yashiro, M., Iwata, C., Morishita, Y., Johansson, E., Matsumoto, Y., Watanabe, A., Aburatani, H., Miyoshi, H., Kiyono, K., et al. (2009). Diffuse-type gastric carcinoma: progression, angiogenesis, and transforming growth factor beta signaling. J. Natl. Cancer Inst. 101, 592–604.

19. Kiyono, K., Suzuki, H.I., Morishita, Y., Komuro, A., Iwata, C., Yashiro, M., Hirakawa, K., Kano, M.R., and Miyazono, K. (2009). c-Ski overexpression promotes tumor growth and angiogenesis through inhibition of transforming growth factor-beta signaling in diffuse-type gastric carcinoma. Cancer Sci. 100, 1809–1816.

20. Peng, Y., Li, X., Liu, H., Deng, X., She, C., Liu, C., Wang, X., and Liu, A. (2020). microRNA-18a from M2 Macrophages Inhibits TGFBR3 to Promote Nasopharyngeal Carcinoma Progression and Tumor Growth via TGFB Signaling Pathway. Nanoscale Res. Lett. 15, 196.

21. Lian, G.Y., Wang, Q.M., Mak, T.S.K., Huang, X.R., Yu, X.Q., and Lan, H.Y. (2021). Inhibition of tumor invasion and metastasis by targeting TGFB-Smad-MMP2 pathway with Asiatic acid and Naringenin. Mol. Ther. Oncolytics 20, 277–289.

22. Takahashi, K., Akatsu, Y., Podyma-Inoue, K.A., Matsumoto, T., Takahashi, H., Yoshimatsu, Y., Koinuma, D., Shirouzu, M., Miyazono, K., and Watabe, T. (2020). Targeting all transforming growth factor-β isoforms with an Fc chimeric receptor impairs tumor growth and angiogenesis of oral squamous cell cancer. J. Biol. Chem. 295, 12559–12572.

23. Li, Y., Xiao, F., Zhang, A., Zhang, D., Nie, W., Xu, T., Han, B., Seth, P., Wang, H., Yang, Y., and Wang, L. (2020). Oncolytic adenovirus targeting TGFB enhances anti-tumor responses of mesothelin-targeted chimeric antigen receptor T cell therapy against breast cancer. Cell. Immunol. 348, 104041.

24. He, F., Feng, G., Ma, N., Midorikawa, K., Oikawa, S., Kobayashi, H., Zhang, Z., Huang, G., Takeuchi, K., and Murata, M. (2022). GDF10 inhibits cell proliferation and epithelial-mesenchymal transition in nasopharyngeal carcinoma by the transforming growth factor-β/Smad and NF-κB pathways. Carcinogenesis 43, 94–103.

25. Zheng, R., Li, F., Li, F., and Gong, A. (2021). Targeting tumor vascularization: promising strategies for vascular normalization. J. Cancer Res. Clin. Oncol. 147, 2489–2505.

26. Minhas, A.S., and Oliver, R. (2022). Magnetic Resonance Imaging Basics. Adv. Exp. Med. Biol. 1380, 47–82.

27. Withey, S.J., Owczarczyk, K., Grzeda, M.T., Yip, C., Deere, H., Green, M., Maisey, N., Davies, A.R., Cook, G.J., Goh, V., et al. (2023). Association of dynamic contrast-enhanced MRI and 18F-Fluorodeoxyglucose PET/CT parameters with neoadjuvant therapy response and survival in esophagogastric cancer. Eur. J. Surg. Oncol. 10, 106934.

28. Jin, T., Jiang, F., Jin, Q.F., Piao, Y.F., and Chen, X.Z. (2018). Endostar Combined with Gemcitabine and Cisplatin Chemotherapy for Patients with Metastatic Nasopharyngeal Carcinoma: an Update. Transl. Oncol. 11, 286–291.

29. Yang, Z., Kang, M., Zhu, S., Huang, J., Li, X., and Wang, R. (2018). Clinical evaluation of vascular normalization induced by recombinant human endostatin in nasopharyngeal carcinoma via dynamic contrast-enhanced ultrasonography. OncoTargets Ther. 11, 7909–7917.

30. Zhang, J., Xue, W., Xu, K., Yi, L., Guo, Y., Xie, T., Tong, H., Zhou, B., Wang, S., Li, Q., et al. (2020). Dual inhibition of PFKFB3 and VEGF normalizes tumor vasculature, reduces lactate production, and improves chemotherapy in glioblastoma: insights from protein expression profiling and MRI. Theranostics 10, 7245–7259.

31. Desert, R., Chen, W., Ge, X., Viel, R., Han, H., Athavale, D., Das, S., Song, Z., Lantvit, D., Cano, L., et al. (2023). Hepatocellular carcinomas, exhibiting intratumor fibrosis, express cancer-specific extracellular matrix remodeling and WNT/TGFB signatures, associated with poor outcome. Hepatology 78, 741–757.

32. Olsen, J., Lefebvre, O., Fritsch, C., Troelsen, J.T., Orian-Rousseau, V., Kedinger, M., and Simon-Assmann, P. (2000). Involvement of activator protein 1 complexes in the epithelium-specific activation of the laminin gamma2-chain gene promoter by hepatocyte growth factor (scatter factor). Biochem. J. 347, 407–417.

33. Harding, J.J., Do, R.K., Yaqubie, A., Cleverly, A., Zhao, Y., Gueorguieva, I., Lahn, M., Benhadji, K.A., Kelley, R.K., and Abou-Alfa, G.K. (2021). Phase 1b study of galunisertib and ramucirumab in patients with advanced hepatocellular carcinoma. Cancer Med. 10, 3059–3067.

34. Courau, T., Nehar-Belaid, D., Florez, L., Levacher, B., Vazquez, T., Brimaud, F., Bellier, B., and Klatzmann, D. (2016). TGFB and VEGF cooperatively control the immunotolerant tumor environment and the efficacy of cancer immunotherapies. JCI Insight 1, e85974.

35. Cowman, S.J., and Koh, M.Y. (2022). Revisiting the HIF switch in the tumor and its immune microenvironment. Trends Cancer 8, 28–42.

36. Segura-Collar, B., Garranzo-Asensio, M., Herranz, B., Hernández-SanMiguel, E., Cejalvo, T., Casas, B.S., Matheu, A., Pérez-Núñez, Á., Sepúlveda-Sánchez, J.M., Hernández-Laín, A., et al. (2021). Tumor-Derived Pericytes Driven by EGFR Mutations Govern the Vascular and Immune Microenvironment of Gliomas. Cancer Res. 81, 2142–2156.

37. Erin, N., Grahovac, J., Brozovic, A., and Efferth, T. (2020). Tumor microenvironment and epithelial mesenchymal transition as targets to overcome tumor multidrug resistance. Drug Resist. Updat. 53, 100715.

38. Dongre, A., and Weinberg, R.A. (2019). New insights into the mechanisms of epithelial-mesenchymal transition and implications for cancer. Nat. Rev. Mol. Cell Biol. 20, 69–84.

39. Zheng, X., Carstens, J.L., Kim, J., Scheible, M., Kaye, J., Sugimoto, H., Wu, C.C., LeBleu, V.S., and Kalluri, R. (2015). Epithelial-to-mesenchymal transition is dispensable for metastasis but induces chemoresistance in pancreatic cancer. Nature 527, 525–530.

40. Okada, Y., Takahashi, N., Takayama, T., and Goel, A. (2021). LAMC2 promotes cancer progression and gemcitabine resistance through modulation of EMT and ATP-binding cassette transporters in pancreatic ductal adenocarcinoma. Carcinogenesis 42, 546–556.

41. Moon, Y.W., Rao, G., Kim, J.J., Shim, H.S., Park, K.S., An, S.S., Kim, B., Steeg, P.S., Sarfaraz, S., Changwoo Lee, L., et al. (2015). LAMC2 enhances the metastatic potential of lung adenocarcinoma. Cell Death Differ. 22, 1341–1352.

42. Cave, D.D., Buonaiuto, S., Sainz, B., Jr., Fantuz, M., Mangini, M., Carrer, A., Di Domenico, A., Iavazzo, T.T., Andolfi, G., Cortina, C., et al. (2022). LAMC2 marks

a tumor-initiating cell population with an aggressive signature in pancreatic cancer. J. Exp. Clin. Cancer Res. 41, 315.

43. Pei, Y.F., Liu, J., Cheng, J., Wu, W.D., and Liu, X.Q. (2019). Silencing of LAMC2 Reverses Epithelial-Mesenchymal Transition and Inhibits Angiogenesis in Cholangiocarcinoma via Inactivation of the Epidermal Growth Factor Receptor Signaling Pathway. Am. J. Pathol. 189, 1637–1653.

44. García-Figueiras, R., Baleato-González, S., Padhani, A.R., Luna-Alcalá, A., Vallejo-Casas, J.A., Sala, E., Vilanova, J.C., Koh, D.M., Herranz-Carnero, M., and Vargas, H.A. (2019). How clinical imaging can assess cancer biology. Insights Imaging 10, 28.

45. Martín-Noguerol, T., Mohan, S., Santos-Armentia, E., Cabrera-Zubizarreta, A., and Luna, A. (2021). Advanced MRI assessment of non-enhancing peritumoral signal abnormality in brain lesions. Eur. J. Radiol. 143, 109900.

46. Gaustad, J.V., Hauge, A., Wegner, C.S., Simonsen, T.G., Lund, K.V., Hansem, L.M.K., and Rofstad, E.K. (2020). DCE-MRI of Tumor Hypoxia and Hypoxia-Associated Aggressiveness. Cancers 12, 1979.

47. Xue, W., Du, X., Wu, H., Liu, H., Xie, T., Tong, H., Chen, X., Guo, Y., and Zhang, W. (2017). Aberrant glioblastoma neovascularization patterns and their correlation with DCE-MRI-derived parameters following temozolomide and bevacizumab treatment. Sci. Rep. 7, 13894.

48. Meng, F., Zou, B., Yang, R., Duan, Q., and Qian, T. (2022). The diagnostic efficiency of the perfusion-related parameters in assessing the vascular disrupting agent (CA4P) response in a rabbit VX2 liver tumor model. Acta Radiol. 63, 1147–1156.

49. Tang, L., Wang, X.J., Baba, H., and Giganti, F. (2020). Gastric cancer and image-derived quantitative parameters: Part 2-a critical review of DCE-MRI and 18F-FDG PET/CT findings. Eur. Radiol. 30, 247–260.

50. Rose, T.A., Jr., and Choi, J.W. (2015). Intravenous Imaging Contrast Media Complications: The Basics That Every Clinician Needs to Know. Am. J. Med. 128, 943–949.

51. Wegner, C.S., Hauge, A., Simonsen, T.G., Gaustad, J.V., Andersen, L.M.K., and Rofstad, E.K. (2018). DCE-MRI of Sunitinib-Induced Changes in Tumor Microvasculature and Hypoxia: A Study of Pancreatic Ductal Adenocarcinoma Xenografts. Neoplasia 20, 734–744.

52. Li, B., Xu, D., Zhou, J., Wang, S.C., Cai, Y.X., Li, H., and Xu, H.B. (2022). Monitoring Bevacizumab-Induced Tumor Vascular Normalization by Intravoxel Incoherent Motion Diffusion-Weighted MRI. J. Magn. Reson. Imaging. 56, 427–439.

53. Le Bihan, D., and Turner, R. (1992). The capillary network: a link between IVIM and classical perfusion. Magn. Reson. Med. 27, 171–178.

54. Nishie, A., Asayama, Y., Ishigami, K., Ushijima, Y., Takayama, Y., Okamoto, D., Fujita, N., Tsurumaru, D., Togao, O., Sagiyama, K., et al. (2019). Amide proton transfer imaging to predict tumor response to neoadjuvant chemotherapy in locally advanced rectal cancer. J. Gastroenterol. Hepatol. 34, 140–146.

55. Park, J.E., Kim, H.S., Park, S.Y., Jung, S.C., Kim, J.H., and Heo, H.Y. (2020). Identification of Early Response to Anti-Angiogenic Therapy in Recurrent Glioblastoma: Amide Proton Transfer-weighted and Perfusion-weighted MRI compared with Diffusion-weighted MRI. Radiology 295, 397–406.

56. Krikken, E., Khlebnikov, V., Zaiss, M., Jibodh, R.A., van Diest, P.J., Luijten, P.R., Klomp, D.W.J., van Laarhoven, H.W.M., and Wijnen, J.P. (2018). Amide chemical exchange saturation transfer at 7 T: a possible biomarker for detecting early response to neoadjuvant chemotherapy in breast cancer patients. Breast Cancer Res. 20, 51.

57. Zhou, J., Zhu, H., Lim, M., Blair, L., Quinones-Hinojosa, A., Messina, S.A., Eberhart, C.G., Pomper, M.G., Laterra, J., Barker, P.B., et al. (2013). Three-dimensional amide proton transfer MR imaging of gliomas: Initial experience and comparison with gadolinium enhancement. J. Magn. Reson. Imaging. 38, 1119–1128.

58. Loi, L., Zimmermann, F., Goerke, S., Korzowski, A., Meissner, J.E., Deike-Hofmann, K., Stieber, A., Bachert, P., Ladd, M.E., Schlemmer, H.P., et al. (2020). Relaxation-compensated CEST (chemical exchange saturation transfer) imaging in breast cancer diagnostics at 7T. Eur. J. Radiol. 129, 109068.

59. Li, L., Chen, W., Yan, Z., Feng, J., Hu, S., Liu, B., and Liu, X. (2020). Comparative Analysis of Amide Proton Transfer MRI and Diffusion-Weighted Imaging in Assessing p53 and Ki-67 Expression of Rectal Adenocarcinoma. J. Magn. Reson. Imaging. 52, 1487–1496.

60. Li, L., Wei, J.R., Dong, J., Lin, Q.G., Tang, H., Jia, Y.X., Tan, W., Chen, Q.Y., Zeng, T.T., Xing, S., et al. (2021). Laminin γ2-mediating T cell exclusion attenuates response to anti-PD-1 therapy. Sci. Adv. 7, eabc8346.

61. Fu, R., Li, Y., Jiang, N., Ren, B.X., Zang, C.Z., Liu, L.J., Lv, W.C., Li, H.M., Weiss, S., Li, Z.Y., et al. (2020). Inactivation of endothelial ZEB1 impedes tumor progression and sensitizes tumors to conventional therapies. J. Clin. Invest. 130, 1252–1270.

62. Radzikowska, J., Krzeski, A., Czarnecka, A.M., Klepacka, T., Rychlowska-Pruszynska, M., Raciborska, A., Dembowska-Baginska, B., Pronicki, M., Kukwa, A., Sierdzinski, J., and Kukwa, W. (2021). Endoglin Expression and Microvessel Density as Prognostic Factors in Pediatric Rhabdomyosarcoma. J. Clin. Med. 10, 512.

63. Kim, S.H., Lee, H.S., Kang, B.J., Song, B.J., Kim, H.B., Lee, H., Jin, M.S., and Lee, A. (2016). Dynamic Contrast-Enhanced MRI Perfusion Parameters as Imaging Biomarkers of Angiogenesis. PLoS One 11, e0168632.

64. Hu, S., Zhang, C., Ni, L., Huang, C., Chen, D., Shi, K., Jin, H., Zhang, K., Li, Y., Xie, L., et al. (2020). Stabilization of HIF-1α alleviates osteoarthritis via enhancing mitophagy. Cell Death Dis. 11, 481.

65. Cai, X.Y., Ni, X.C., Yi, Y., He, H.W., Wang, J.X., Fu, Y.P., Sun, J., Zhou, J., Cheng, Y.F., Jin, J.J., et al. (2016). Overexpression of CD39 in hepatocellular carcinoma is an independent indicator of poor outcome after radical resection. Medicine (Baltim.) 95, e4989.

66. Ray, K.J., Simard, M.A., Larkin, J.R., Coates, J., Kinchesh, P., Smart, S.C., Higgins, G.S., Chappell, M.A., and Sibson, N.R. (2019). Tumor pH and Protein Concentration Contribute to the Signal of Amide Proton Transfer Magnetic Resonance Imaging. Cancer Res. 79, 1343–1352.

67. Pan, J.H., Zhu, S., Huang, J., Liang, J., Zhang, D., Zhao, X., Ding, H., Qin, L., Shi, C., Luo, L., and Pan, Y. (2018). Monitoring the Process of Endostar-Induced Tumor Vascular Normalization by Non-contrast Intravoxel Incoherent Motion Diffusion-Weighted MRI. Front. Oncol. 8, 524.